

Synchronized Ratiometric Codelivery of Metformin and Topotecan through Engineered Nanocarrier Facilitates In Vivo Synergistic Precision Levels at Tumor Site

Venkatesh Teja Banala, Shweta Sharma, Puja Barnwal, Sandeep Urandur, Ravi P. Shukla, Naseer Ahmad, Naresh Mittapelly, Gitu Pandey, Monika Dwivedi, Navodayam Kalleti, Kalyan Mitra, Srikanta Kumar Rath, Ritu Trivedi, and Prabhat Ranjan Mishra*

The combination of metabolic modulators with chemotherapy holds vast promise for effective inhibition of tumor progression and invasion. Herein, a ratiometric codelivery platform is developed for metformin (MET), a known metabolic modulator and topotecan (TPT), a chemotherapeutic drug, by engineering lipid bilayer–camouflaged mesoporous silica nanoparticles (LB-MSNs). In an attempt to deliver and maintain high tumor site concentrations of MET and TPT, a novel ion pairing–assisted loading procedure is developed using pamoic acid (PA) as an in situ trapping agent. PA, a hydrophobic counterion, increases the hydrophobicity of MET and TPT and facilitates MSNs with exceptionally high payload capacity (>40 and 32 wt%, respectively) and controlled release profile. Further, the synergy between MET and TPT determined by a modeling approach helps to afford synchronized delivery of both the drugs. Coloaded MET and TPT LB-MSNs present synergistic cytotoxicity against MDA-MB-231/4T1 cells and effectively promote apoptosis via mitochondrial membrane depolarization and cell cycle arrest. Extended pharmacokinetic profiles in preclinical models with fourfold to sevenfold longer circulation half-life and 7.5–100 times higher tumor site concentrations correspond to a significant increase in pharmacodynamic efficacy. Taken together, the developed codelivery approach effectively addresses the challenges in the chemotherapeutic efficacy of MET and TPT collectively.

fatal malignancies among women globally. Progressively more failures of surgical resection, radiotherapy, also hormone therapy, owing to the desensitization of receptors, had raised disquieting ultimatum. The clinical benefits of hormone therapy are limited due to the common issues like drug resistance, dose limited toxicity, and harsh tumor microenvironment that hinder the drug penetration and efficacy.^[1] Thus, growing obligation in terms of complexity in treatment manifests the inception of hormone refractory breast cancer. Due to the physiological complexity of the tumor, monotherapy strategies are found to be not effective with more relapse rates which led to an interest in combination chemotherapy regimens, referring to the simultaneous administration of two or more drugs for achieving long-term prognosis with less unwanted side effects.^[2] Unlike monotherapy, combination chemotherapies may cause synergistic response, maximize the therapeutic effect, and overcome drug resistance by modulating different signaling pathways in cancer

cells. With the increase in understanding of molecular pathways, tumor microenvironment, and host–tumor interactions, new combination therapies are continuously evolving with new paradigms.^[2b,3] Combination therapy with drugs that enable

1. Introduction

Conceding to the shortcomings of contemporary management stratagems, breast cancer exults as one of the most frequent and

V. T. Banala, Dr. S. Sharma, P. Barnwal, S. Urandur, R. P. Shukla, N. Mittapelly, G. Pandey, Dr. M. Dwivedi, Dr. P. R. Mishra
Division of Pharmaceutics and Pharmacokinetics
CSIR–Central Drug Research Institute
Lucknow 226031, India
E-mail: prabhat_mishra@cdri.res.in, mishrapr@hotmail.com
N. Ahmad, Dr. R. Trivedi
Division of Endocrinology
CSIR–Central Drug Research Institute
Lucknow 226031, India

N. Kalleti, Dr. S. K. Rath
Division of Toxicology
CSIR–Central Drug Research Institute
Lucknow 226031, India
Dr. K. Mitra
Electron Microscopy Division
CSIR–Central Drug Research Institute
Lucknow 226031, India

DOI: 10.1002/adhm.201800300

metabolic reprogramming is one such approach gaining more clinical prominence in recent years by addressing chemoresistance and safety concerns tangled in standard chemotherapies.^[4]

Recent studies have shown that metformin (MET), a common antidiabetic drug and promising anticancer metabolic modulator, demonstrated significant growth inhibition and proapoptotic effects in several cancers, including breast cancer.^[5] MET activates 5' adenosine monophosphate-activated protein kinase (AMPK), inhibits the mammalian target of rapamycin (mTOR), and downregulates excision repair cross-complementation group 1 (ERCC1).^[6] Retrospective studies have reported that patients with diabetes receiving MET exhibited decreased cancer incidence and cancer-related mortality.^[7] Various early stage clinical trials are presently underway to probe metformin's potential to combat an array of cancers, including colorectal, prostate, endometrial, and breast cancer.^[5a] However, clinical progress of MET as a treatment regimen has been constrained by its rapid elimination, high aqueous solubility, and subtherapeutic tumor site concentrations.^[8]

Interestingly, several preclinical studies have shown that MET exerts synergistic effects in combination with various classes of chemotherapeutic agents, like hormone modulation, antimetabolite, antibiotics, and drugs that affect structure and function of DNA.^[9] Having realized that MET could show synergistic effects in combination with topoisomerase inhibitors,^[10] in this study, we explored the combination therapy of MET with topotecan (TPT) against breast cancer. TPT is a semisynthetic analog of camptothecin suppressing DNA replication by inhibiting the nuclear enzyme topoisomerase I. TPT has been licensed to be a second line anticancer agent for small cell lung cancer (SCLC)^[11] and ovarian cancer.^[12] In addition to its cytotoxic activity against solid tumors, TPT has shown potential activity against metastases from breast cancer^[13] and SCLC^[14] in numerous clinical reports.

Theoretically, the success of combination chemotherapy in cancer majorly depends on the ratios of individual agents at the tumor site. Accounting to the dissimilar pharmacokinetic profiles of individual drugs, meager penetration, and heterogeneous distribution, the redemption of actual synergistic ratios at the target site confronted issues to realize the ultimate therapeutic effect of the regimen.^[15] To mitigate the problems associated with free drug combination therapy, nanoparticles have formulated to coload synergistic drug combinations.^[16] Delivery of synergistic drug ratios through nanocarriers provides controlled, temporal, and spatial delivery of multiple cargos, enables drug accumulation in tumor, and releases the drugs at a synchronized rate, thereby, probability of maintenance of intracellular synergistic drug concentrations is possible.^[15c,17] But, coencapsulation of multiple drugs with different physicochemical properties in the same nanocarrier and controlling the drug release are always challenging tasks.^[18] Appropriate physical and chemical engineering of the nanoparticles are needed to enable optimal loading of multiple drugs and by imparting adjustable release kinetics to the delivery vehicle commensurate the required concentration–time profile at the site of action.^[19]

Herein, we describe the coencapsulation of MET and TPT in a lipid bilayer-coated mesoporous silica nanoparticles (LB-MSNs) with an aim to achieve high payload and controlled release profile. Among candidate nanocarriers, MSNs offers many

advantages over polymeric and lipidic delivery systems, such as uniform controlled particle size and shape with high surface area and modifiable surface chemistry which can widely accommodate high payloads of disparate cargos.^[20] However, MSNs often require coatings to shield the surface silanol groups that are highly lipophilic and known to promote nonspecific binding and mononuclear phagocytic system (MPS) uptake.^[21] In this context, lipid bilayer-coated MSNs have unique attributes which combine the advantages of liposomes with MSNs. To date, several studies reported the effective delivery of multiple classes of drugs and drug combinations using lipid bilayer-supported MSNs with excellent in vitro and in vivo results.^[22] Since, MET is a highly water-soluble drug (>300 mg mL⁻¹), conventional polymeric and lipidic nanoparticulate systems fail in achieving reasonable payload efficiency. Our initial trials with PLGA nanoparticle could be able to accommodate less than 5% w/w of MET with rapid release within 8 h (data not shown). Although liposomal system exhibited efficient loading, inherent stability and burst release drawn obscure inferences for the liposomal system.^[23] To overcome these challenges, we developed a novel hydrophobic ion trapping-assisted loading of MET and TPT using pamoic acid (PA) as in situ ion trapping agent. The large surface area of MSNs enables to achieve a high payload of both the drugs and in situ ion trapping offers reasonable hydrophobicity to MET, whereas, TPT exhibited protagonist for controlling the release. The in vitro synergy evaluation between MET and TPT using modeling approach is a major highlight of the study, where the derived ratiometric payload of drugs was delivered and evaluated for enhancement of total efficacy of plain drugs in comparison to the mixture of nanoparticles and coloaded nanoparticles. Additionally, pharmacokinetic studies and intratumoral drug concentrations were determined as a measure of maintenance of synergistic drug ratios and local drug bioavailability. The pharmacodynamic capability of the designed approach was evaluated in 4T1 tumor-bearing mouse model. Overall, this work illustrates the example of how to rationally design and coencapsulate highly water-soluble drugs with controlled release, how modifying the drug loading conditions can affect drug coencapsulation and provides insights on designing combination chemotherapy studies for assessing drug synergism in vitro and in vivo.

2. Results and Discussion

2.1. Coencapsulation of MET and TPT in Lipid Bilayer-Coated Mesoporous Silica Nanoparticles Using PA as In Situ Hydrophobic Ion Pairing (HIP) Agent

In this study, we have selected two water-soluble drugs, MET and TPT for the coencapsulation into the MSNs. Here, we took a major challenge to entrap highly water-soluble MET (>300 mg mL⁻¹) into the MSNs with an objective to control the release reasonably for a duration of 24–48 h. To achieve this goal, we have used PA as novel in situ hydrophobic ion trapping agent (HIP) for high drug loading and controlled release. To understand the HIP formation, metformin pamoate (MET-PA) and topotecan pamoate (TPT-PA) salts were synthesized and confirmed with ¹H-NMR (see the Supporting Information for a detailed discussion). From the equilibrium solubility experiments, it was clear

that aqueous solubility of HIPs was ≈ 40 -fold and ≈ 7.7 -fold lower for MET-PA and TPT-PA, respectively, in comparison to plain drugs (Figure S1D,F, Supporting Information).

Although HIP formation is confirmed, one major challenge in loading MET is its low permeability across lipid bilayer due to its ionic nature and high pK_a (>12.4). Based on various reports and evidences stating the ionic transport of drugs, we have performed transwell artificial membrane permeability assay for MET at different temperature and pH conditions.^[24] It was observed that the effective permeability of MET was increased from fivefold to 28-fold with an increase in temperature and pH (Figure S2A1, Supporting Information). After understanding the positive effects of pH and temperature on the permeability of MET, we proceed to develop an active loading approach using PA as ion trapping agent. Initially, we have encapsulated MET and TPT individually into LB-MSNs. The passive entrapment of the MET and TPT into the cores of MSNs achieved a loading efficiency of 18 and 15 wt%, respectively. In our preliminary examination, it was found that plain MET-loaded MSNs could not sustain the drug release due to the high aqueous solubility. With an aim to load further high amount of drug with a controlled release, we have developed a novel remote loading technique. To the best of our knowledge, this is the first report of using in situ hydrophobic ion pairing for high drug loading of water-soluble drugs.

To develop remote loading procedure we used PA-loaded LB-MSNs, (PA)LB-MSNs, composed of SoyaPC/cholesterol/1,2-distearoyl-sn-glycero-3-phosphoethanolamine-polyethylene glycol-₂₀₀₀ (DSPE-PEG₂₀₀₀) at a molar ratio of 7:2.75:0.25 (Figure 1A). The (PA)LB-MSNs were incubated in 10 mg mL⁻¹ of MET and 1 mg mL⁻¹ of TPT drug solutions. The gradient and electrochemical potential across the lipid membrane and other factors like pH and incubation temperature allow the drug to drive inside the MSNs and get entrapped inside the pores as HIP after precipitating with the counterion, PA (Figure 1B). Different loading parameters were employed to achieve efficient loading. For MET, an optimum pH 9 was maintained outside the MSNs. Although MET exists in ionic form, pH 9 was selected to prevent the harsh environment. For TPT, being an amphipathic base pH 7.4 was found sufficient to maintain the gradient for the remote loading into MSNs. Under defined conditions, we able to achieve a maximum loading of ≈ 40 wt % for MET and ≈ 32 wt% for the TPT. The coloaded was performed under the conditions of MET by which we have achieved around 35 wt% of MET and 10 wt% of TPT. For all the formulations, we have selected an optimum 4 h of incubation time for efficient loading.

Although we have achieved a maximum loading up to 35–40%, we have chosen to load 25% of MET and 0.5% of TPT based on efficient synergy achieved in in vitro modeling studies. To achieve 25/0.5 wt% ratio of loading, we have used 5 mg mL⁻¹ of MET and 0.08 mg mL⁻¹ of TPT solutions with triethylamine (TEA) as gradient ion for loading.

2.1.1. Physicochemical Characterization of LB-MSNs

Size measurements by DLS technique revealed that the particle size of LB-MSNs was 97.33 ± 5.63 nm, upon loading of PA, the size was slightly increased to 110 ± 8.85 nm. No significant change in size was observed before and after drug loading of

MET and TPT with in situ HIP approach (MP)LB-MSNs, (TP) LB-MSNs, and coloaded MSNs, (MP+TP)LB-MSNs. This is again confirmed by the transmission electron microscopy which reveals a uniform intact coating of the lipid bilayer (Figure 2A).

Zeta potential measurements of plain MSNs, LB-MSNs, (MP) LB-MSNs, (TP)LB-MSNs, and coloaded (MP+TP)LB-MSNs were shown in Figure 2A. There is a marked difference in zeta potential observed in plain and LB-MSNs which is an indirect confirmation of the intact coating of the lipid bilayer. Drug loading procedures did not affect the zeta potential of the formulations.

To confirm the in situ HIP formation after drug loading, MSNs were evaluated by infrared spectroscopy (Figure 2B). The characteristic peaks at 3466 (O–H stretch), 3166 (N–H stretch), 2927 (N–H stretch), 1640 (C=O stretch), 1507 (C=O stretch), and 1269 cm⁻¹ of MET-PA salt were also observed on (MP)LB-MSNs and (MP+TP)LB-MSNs, confirming the formation of HIP inside MSNs. Similarly TPT-PA characteristic peaks 3402 (O–H stretch), 2978 (C–H stretch), 2879 (C–H stretch), 1740 (C=O stretch), 1651 (C=N aromatic stretch), 1590 (C=C aromatic bend), 1506 (C=O stretch), and 1160 cm⁻¹ (C–N stretch) were observed in (TP)LB-MSNs and (MP+TP)LB-MSNs. As can be seen clearly, Fourier-transform infrared (FT-IR) spectra of MSNs with PA salts of both MET and TPT closely match with the respective salts (MET-PA and TPT-PA). This confirms the in situ HIP formation between active pharmaceutical ingredient (API) and counterion similar to that of solid salts.

2.1.2. Evaluation of Key Drug Loading Parameters of the Counterion on Drug Loading Efficiency

As a part of the study, we have also evaluated basic parameters such as the type of gradient ion, pH, and temperature that could affect the drug loading efficiency. We have evaluated three gradient ions of PA, sodium, ammonium, and TEA. All the gradient ion concentrations were kept constant at 10×10^{-3} M equimolar concentration of PA throughout the experiment. From the results, it was evident that TEA (42 wt%) was most efficient gradient ion followed by ammonia (32 wt%) and sodium ions (28 wt%) Figure 2C. Apart from this, pH of the outer phase is a critical parameter which affects the gradient required for the influx of drug into MSNs. Both the drugs behaved in a different manner with the pH, since MET is highly ionic in nature, we expected low drug loading into MSNs, but conversely, we observed a better drug loading of MET than TPT, increase in the pH resulting in a slight improvement in loading.

We also considered temperature and duration of incubation on the drug loading. The temperature was found to have a profound effect on drug loading capability for both the drugs. A temperature of 55–60 °C was found to be suitable with an optimum 4 h of incubation time for efficient drug loading (Figure 2C). Increase in drug loading may be due to increased lipid bilayer permeability and higher pore volume at higher temperatures.

2.1.3. In Vitro Drug Release Studies

To evaluate the efficiency of the developed formulation, in vitro drug release studies were performed for (MP)LB-MSNs,

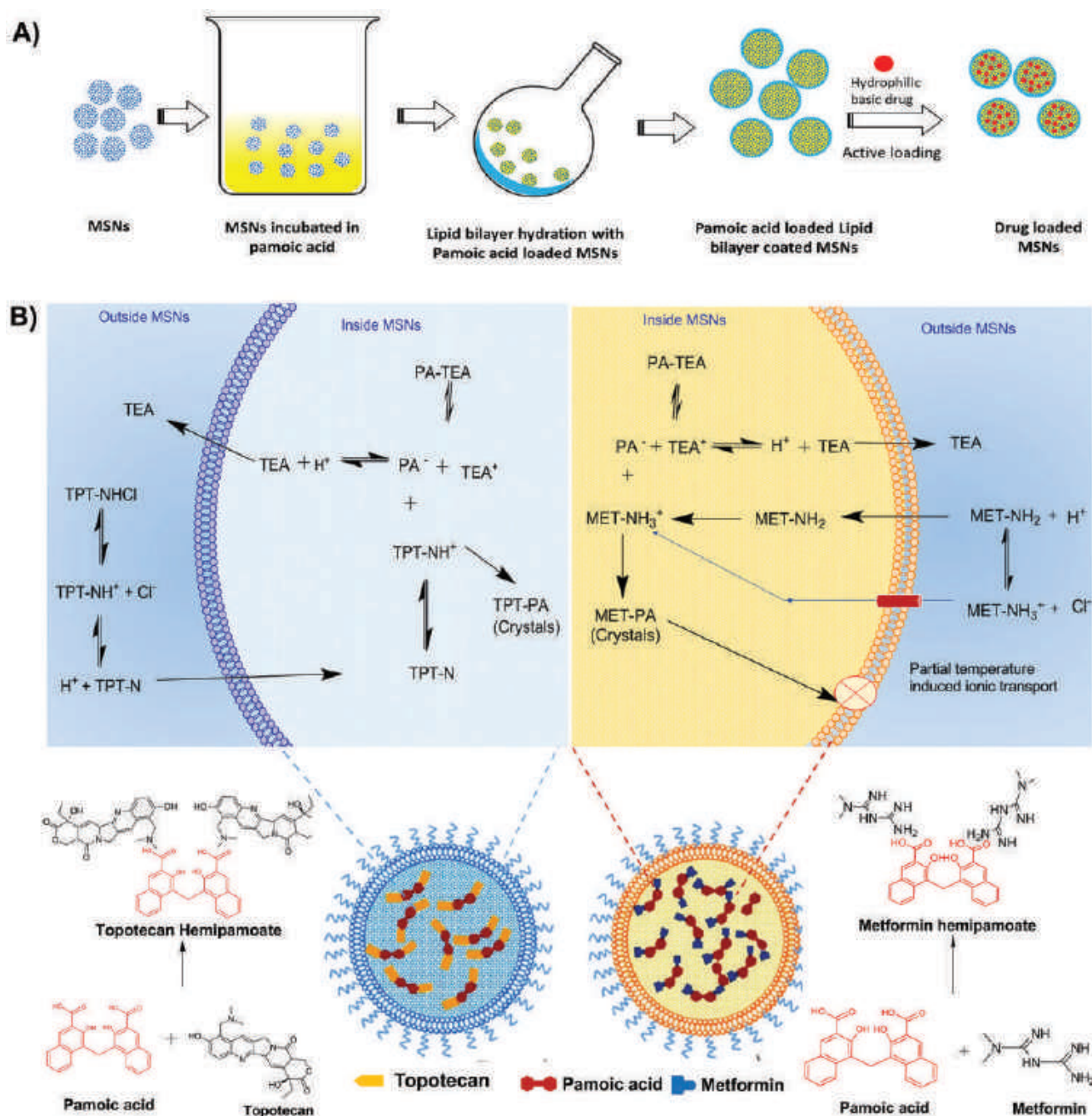


Figure 1. A) Schematics depicting the stepwise preparation of LB-MSNs. B) Mechanistic representation of active loading procedure in PA-loaded LB-MSNs, TEA salt of PA present inside the LB-MSNs allows basic drugs into the MSNs due to gradient difference across the membrane. In case of MET, the higher temperatures partially influence the lipid bilayer permeability. Basic drug after reaching inside MSNs reacts with PA and forms a hydrophobic ion pair (HIP) inside MSN.

(TP)LB-MSNs, and coloaded MSNs with and without trapping agent at two different pH 7.4 and 5.5 to simulate blood and tumor microenvironment, respectively. (MP)LB-MSNs showed sustained release up to 48 h with a cumulative drug release of 95% at pH 5.5 and 86.5% at pH 7.4 (Figure 2D). However, drug release from (TP)LB-MSNs was slower than (MP)LB-MSNs, where 76% and 52% of cumulative TPT release was observed at pH 5.5 and 7.4 within 48 h (Figure 2D). No significant

difference in release was observed in the coloaded formulation (MP+TP)LB-MSNs compared to individual drug-loaded formulations. The differential release of MET and TPT from the formulation with trapping agent may be attributed to the difference in hydrophobicities of in situ formed HIPs, MET-PA and TPT-PA, where the solubility of MET-PA (7.4 mg mL⁻¹) was relatively more compared to TPT-PA (0.16 mg mL⁻¹). It was also observed that coloaded formulation without trapping

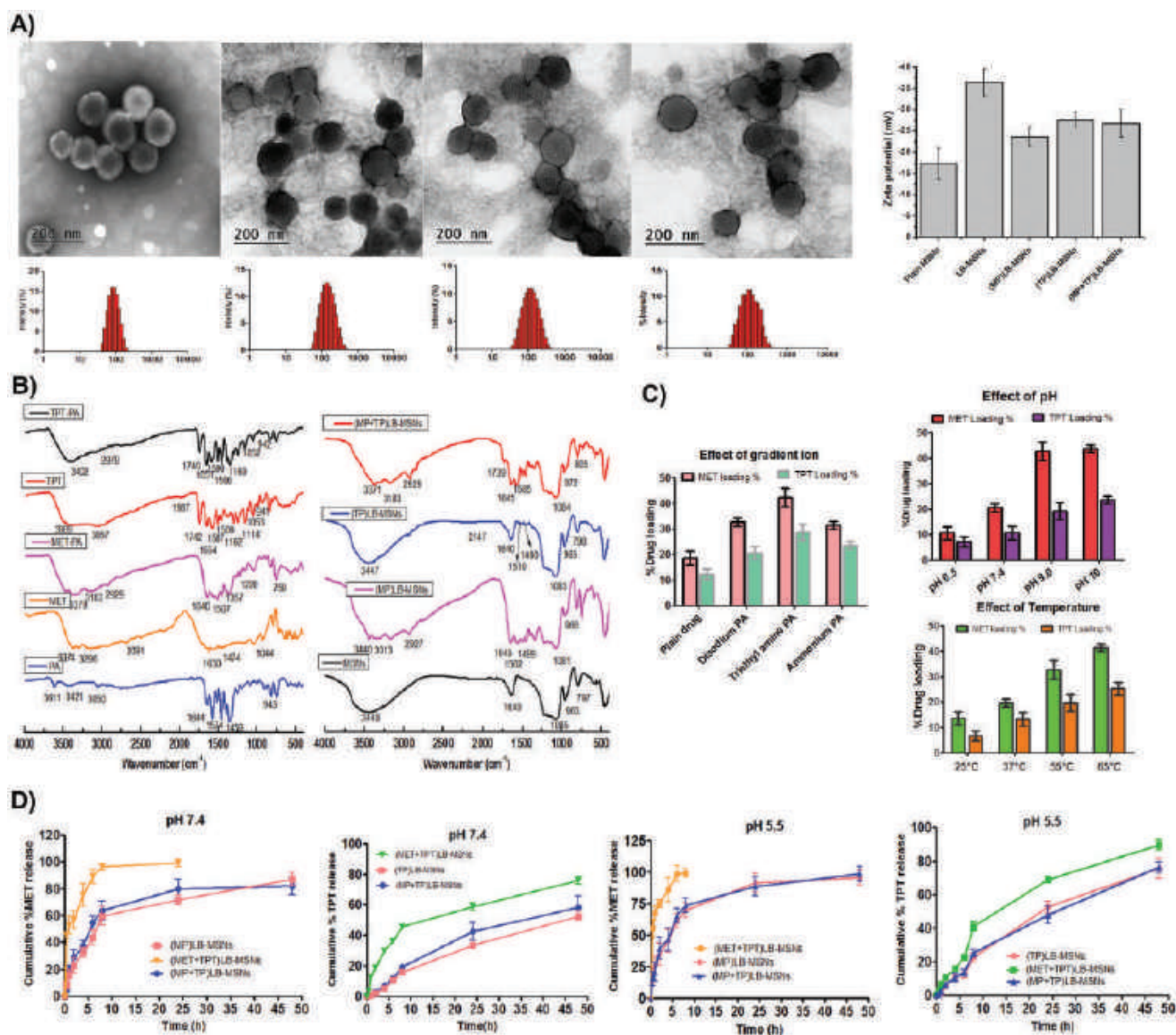


Figure 2. A) Size and polydispersity index (PDI) data of different MSNs, images of transmission electron microscopy (TEM) and dynamic light scattering (DLS) of LB-MSNs, (MP)LB-MSNs, (TP)LB-MSNs, (MP+TP)LB-MSNs (from left to right), and change in zeta potential of different formulations. B) FT-IR of single components (MET, TPT, PA), MET-PA, TPT-PA salts, blank MSNs, and MSNs containing MET, TPT, and PA. C) Various factors affecting the drug loading efficiency; effect of pH, effect of type of gradient ion, and effect of temperature. D) In vitro cumulative percent drug release profiles of MET and TPT from various MSN formulations at pH 7.4 and pH 5.5. All data are expressed as mean \pm SD ($n = 3$).

agent, (MET+TPT)LB-MSN was unable to control the release of MET from the MSNs (75% drug release in 4 h at pH 7.4). But, TPT release was comparatively controlled from MSNs without trapping agent (36.6% in 6 h at pH 7.4) which may be due to inherent lipophilic interactions toward silanol groups of MSNs.

The use of LB-MSNs as a delivery vehicle and in situ HIP formation substantially increase the release time of MET which is a major challenge. Using LB-MSNs, Liu et al. reported irinotecan delivery, in which fivefold increase tumor distribution and 11-fold increase in plasma half-life with a controlled in vivo release of more than 48 h were achieved.^[25] Similarly, Meng et al. successfully codelivered gemcitabine and paclitaxel in synergistic ratios using lipid bilayer-coated MSNs with a

controlled release of water soluble gemcitabine for more than 48 h, in vitro.^[26] In comparison to similar delivery systems, present results substantiate its efficacy as a codelivery platform to achieve synergistic tumor site concentrations.

2.2. In Vitro Cell Culture Studies

2.2.1. Identification of Effective Synergy Combinations between MET and TPT Using Mathematical Modeling

To evaluate the combined effects of MET and TPT, 6×6 concentration combination experiments were performed in

MDA-MB-231 and 4T1 cell lines using 3-(4,5-dimethylthiazol-2-yl)-2,5-diphenyltetrazolium bromide (MTT) assay after 48 h treatment. We have investigated concentration ranges, $0.01 \times 10^{-3} - 5 \times 10^{-3}$ M of MET and $0.01 \times 10^{-6} - 5 \times 10^{-6}$ M of TPT. After MTT treatment and obtaining the growth inhibition data, we have used COMBENFIT software package to objectively identify the synergistic combinations of MET and TPT. We assessed the region of the synergy of each combination independently with three established mathematical models, such as Bliss, Loewe, and highest single agent (HSA) models.^[27] Particulars of these models and their relative advantages can be

found in previous publications.^[28] From the modeling data, we identified that effective synergy was present with $0.05 \times 10^{-3} - 0.5 \times 10^{-3}$ M of MET and $0.1 \times 10^{-6} - 1 \times 10^{-6}$ M of TPT in both the cell lines (Figure 3A and Figure S4A (Supporting Information)). The analysis of single-agent effect reveals, that inhibitory concentration (IC₅₀) (IC₅₀) of MET and TPT was 3.95×10^{-3} M and 1.15×10^{-6} M, respectively, in MDA-MB-231 cell line and 3.59×10^{-3} M and 1.01×10^{-6} M in 4T1 cell line, respectively (Figure 3C and Figure S4C (Supporting Information)).

After identification of the synergy combinations, we tried to analyze the same with the developed formulations. We

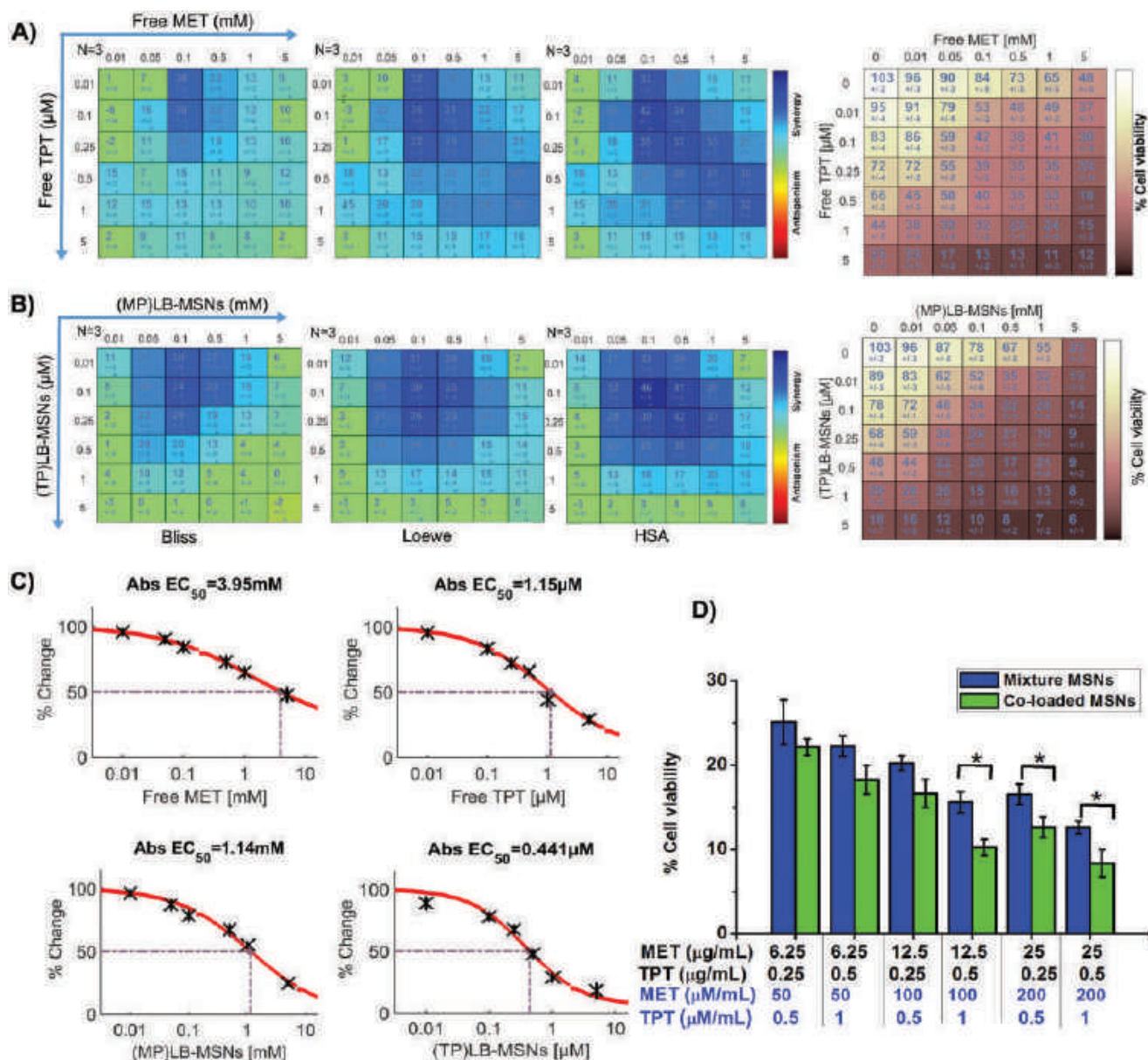


Figure 3. Predicted inhibition data of the three synergy models [Bliss, Loewe, highest single agent (HSA)] in MDA-MB-231 cells treated with A) free MET (x-axis) and free TPT (y-axis), B) (MP)LB-MSNs (x-axis) and (TP)LB-MSNs (y-axis) in 6 × 6 concentration checkerboard format for 48 h using MTT assay. All data are expressed as mean ± SD, $n = 3$, $*p \leq 0.05$; $**p \leq 0.01$; the synergy spots are represented blue in the matrix and experimental data of growth inhibition compared with control are presented. C) Single-agent effect IC₅₀ of the individual drug and drug-loaded LB-MSNs. D) Comparative growth inhibition data of the coloaded and mixture formulations in definite ratios. All data are expressed as mean ± SD, $n = 3$, $*p \leq 0.05$.

repeated the same experiment with a mixture of individual drug-loaded LB-MSNs, i.e., (MP)LB-MSNs and (TP)LB-MSNs in the drug equivalent ratios. After data treatment, we found a good enhancement in the representative synergistic score of the individual models with a significant reduction in the individual IC₅₀ values (Figure 3B and Figure S4B (Supporting Information)). It was found that IC₅₀ of (MP)LB-MSNs and (TP)LB-MSNs was reduced to 1.14×10^{-3} and 0.44×10^{-6} M, 1.33×10^{-3} and 0.40×10^{-6} M in MDA-MB-231 and 4T1 cell lines, respectively (Figure 3C and Figure S4C (Supporting Information)). IC₅₀ of encapsulated drugs were 35–50% lower than free drugs. From the data, it was also clear that synergy was present with 0.05×10^{-3} – 1×10^{-3} M of MET and 0.1×10^{-6} – 1×10^{-6} M of TPT.

To observe the cytotoxicity of the drug-free MSNs, we carried out the cell viability studies for blank LB-MSNs and (PA) LB-MSNs up to 5 mg mL⁻¹ concentration in MDA-MB-231 and 4T1 cell lines. From the results (Figure S3, Supporting Information), it was clear that drug-free LB-MSNs and pamoic acid-loaded LB-MSNs, and (PA)LB-MSNs did not exert cytotoxic effects at the experimental concentrations of in vitro studies.

Based on these modeling data, practical formulation, and dosing aspects, we tried to rationally design the coloaded LB-MSNs. Initially, we have selected six combinations of MET/TPT (50/0.5, 50/1, 100/0.5, 100/1, 200/0.5, and 200/1 of MET/TPT ($\times 10^{-6}$ M)). From the MTT assay, it was observed that coloaded formulations were proven furthermore efficacious compared to a mixture of individual formulations (Figure 3D). Considering the practical loading aspects in MSNs and clinically relevant dosing, we have selected 200/1 (in $\times 10^{-6}$ M) molar ratio of MET/TPT for in vivo studies which meets the practical loading of 25 (wt%) MET and 0.5 (wt%) TPT loading.

2.2.2. Cell Uptake Studies

To evaluate the codelivery efficiency of the LB-MSNs, cellular uptake behavior was monitored in MDA-MB-231 cells using confocal microscopy. To test the hypothesis that the coloaded nanoparticles ensure the deterministic delivery of both cytotoxic drugs versus stochastic distribution in a mixture of nanoparticles, we engineered nanoparticles tagged with fluorescein isothiocyanate (FITC) (green) or rhodamine B, (Red) tracers. MDA-MB-231 cells were incubated with either a combination of FITC-loaded LB-MSNs, (FITC)LB-MSNs, and rhodamine B-loaded LB-MSNs, (RhB)LB-MSNs, or coloaded MSNs, (FITC+RhB)LB-MSNs which contain both the tracers. Interestingly, confocal microscopy revealed that while a large fraction of cells internalizes both the nanoparticles, there was certain cell population that took up either FITC or RhB particles alone (Figure S5, Supporting Information).

2.2.3. Codelivery of MET and TPT Enhances Induction of Cell Cycle Arrest and Apoptosis via Alteration in Mitochondrial Membrane Potential

To further evaluate the intracellular effects of various formulations loaded with MET and TPT alone and in combination, cell

cycle analysis, mitochondrial membrane potential, and apoptosis studies were performed using flow cytometric analysis. In cell cycle analysis, the nuclear content of the treated cells was quantified on the basis of propidium iodide (PI) signals and mitochondrial membrane depolarization was measured with the help of JC-1 dye. To quantify the apoptosis, widely used Annexin-V FITC binding-based flow cytometric assay was performed. It is well known that apoptosis occurs by two pathways: the death receptor-mediated and mitochondrial pathways.^[29] It is widely studied that mitochondrial depolarization is one of the major pathway involved in the apoptosis induced by MET^[30] and TPT.^[31] As illustrated in **Figure 4**, the treatment with MET and TPT alone and in combination induced mitochondrial membrane depolarization that leads to cell cycle arrest and subsequently apoptosis. MSNs loaded with MET and TPT, [(MP)LB-MSNs, (TP)LB-MSNs, and (MP+TP)LB-MSNs] further enhanced the apoptotic effects via mitochondrial membrane depolarization in a synergistic manner. Quantitatively, free MET and TPT induce mitochondrial depolarization in 14.03% and 15.01% cell population, respectively. But, in combination treatment with free drugs slightly enhanced the population which was observed to be antagonistic. Drug-loaded LB-MSNs significantly enhanced the depolarization representing 27.08% and 31.03% of cell population for (MP)LB-MSNs and (TP)LB-MSNs, respectively. In combination treatment, coloaded formulation, (MP+TP)LB-MSNs had shown higher depolarization (54.98%) compared to mixture LB-MSNs (42.25%) and Free MET+TPT (20.81%).

As depicted from the cell cycle analysis data, free MET and (MP)LB-MSNs displayed vivid G1 phase arrest via activation of AMPK through upregulation of p53–p21^{waf1} axis.^[32] Whereas free TPT, (TP)LB-MSNs showed prominent G2 phase arrest. Compared to plain TPT (G2-21.89%) (TP)LB-MSNs induced more G2 phase arrest. In combination studies, the effect of MET+TPT showed a pronounced effect compared to individual treatments and it was also observed that MET+TPT combination induced more S phase and G2 phase arrest contrary to G1 phase arrest. Quantitatively, there was more pronounced effects observed in groups of the coloaded formulation (MP+TP) LB-MSNs, (G2-39.84%, S-57.72%), compared to the mixture of drug loaded MSNs (MP)LB-MSNs+(TP)LB-MSNs, (G2-41.5% S-47.46%). In a similar manner subsequent to cell cycle arrest, treatment with coloaded formulation induced more apoptosis compared to the mixture of MSNs loaded with two individual drugs after 48 h of treatment. (MP+TP)LB-MSNs induced 65.52% of apoptosis compared to a mixture of MSNs loaded with individual drugs, 47.94%. This represents that the codelivery of MET and TPT demonstrated collaborative effects on mitochondrial depolarization and cell cycle arrest, resulting in MDA-MB-231 cell apoptosis. This clearly demonstrates that the deterministic delivery of drugs in a single nanoparticle system would be more advantageous compared to a mixture of nanoparticles.

2.3. In Vivo Studies

2.3.1. In Vivo Near Infrared Fluorophore (NIRF) Live Imaging

In order to follow the biodistribution of the LB-MSNs to the tumor site, animals were intravenous (i.v.) injected with

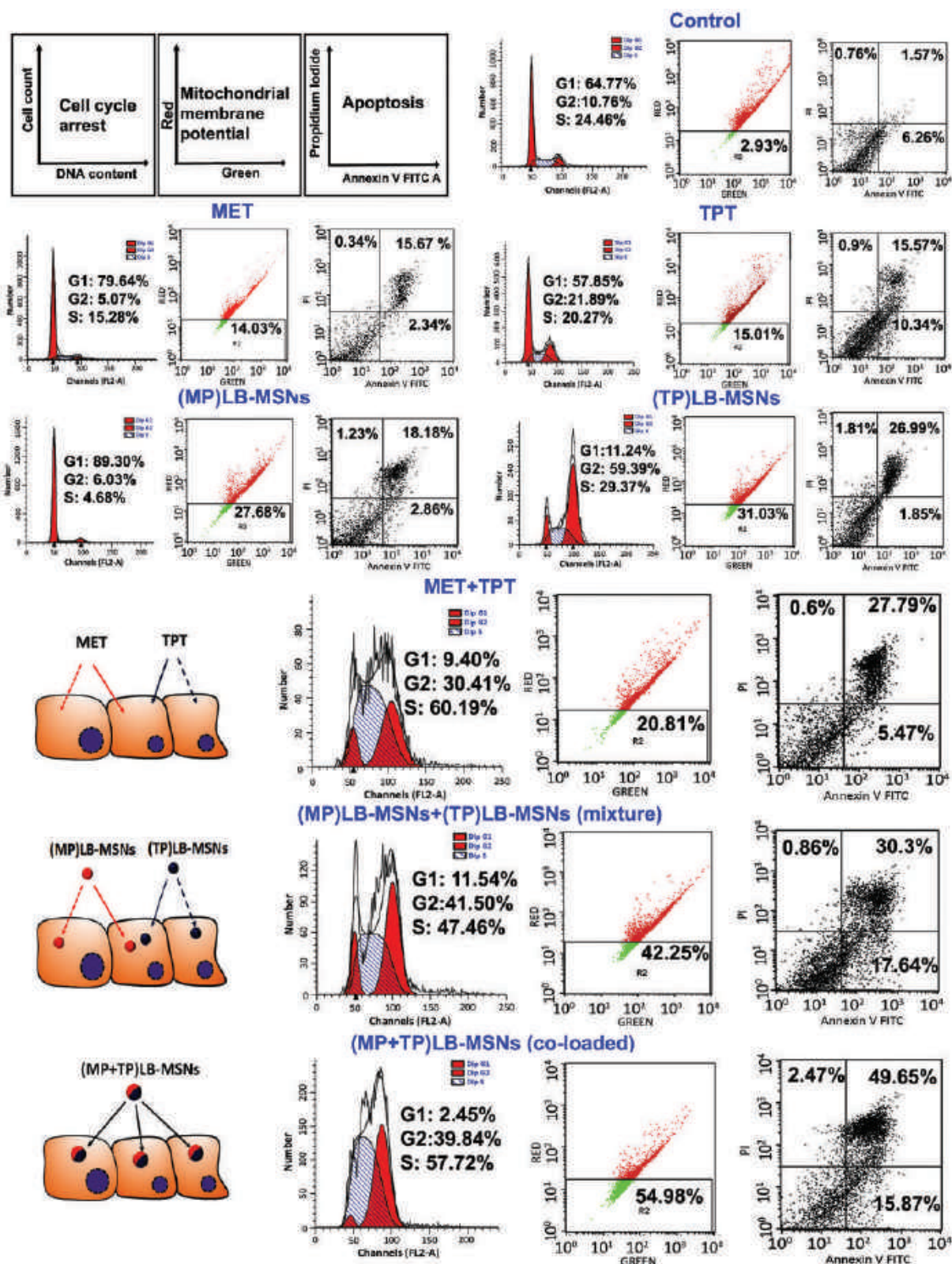


Figure 4. Representative flow cytometry images of cell cycle arrest, mitochondrial membrane potential, and apoptosis showing the combined effect of free MET+TPT and various LB-MSN formulations in MDA-MB-231 cell lines. Cell cycle arrest and mitochondrial membrane potential were performed after 24 h treatment and apoptosis was performed at 48 h with free drugs (MET and TPT) and LB-MSN formulations alone and in combinations. In combination experiments, 200×10^{-6} M of MET and 1×10^{-6} M TPT were used. All results were obtained in triplicate ($n = 3$).

near-infrared (NIR)-labeled (DiR740)LB-MSNs, after achieving the 200–300 mm³ tumor size (Figure 5A). IVIS imaging was obtained prior to and following IV injection of 1 mg kg⁻¹ equivalent, DiR-labeled LB-MSNs at the designated time points. Robust fluorescence intensity was observed at the tumor sites within 4 h of LB-MSN injection, following which the signal was sustained for at least 24 h. This was also confirmed by ex vivo imaging of the tumors and major organs collected from the animals, following sacrifice 24 h postinjection (Figure 5A1,A2). In addition to abundant particle uptake at the tumor site, the

liver and spleen were also major sites of particle distribution. Little signaling was obtained in the lung and kidney.

2.3.2. Pharmacokinetics and Tumor Distribution

To determine the effect of HIP on pharmacokinetics and tumor distribution of MET and TPT, we have compared coloaded particles with and without trapping agent after i.v. administration. Tumor-bearing mice were injected with MET+TPT

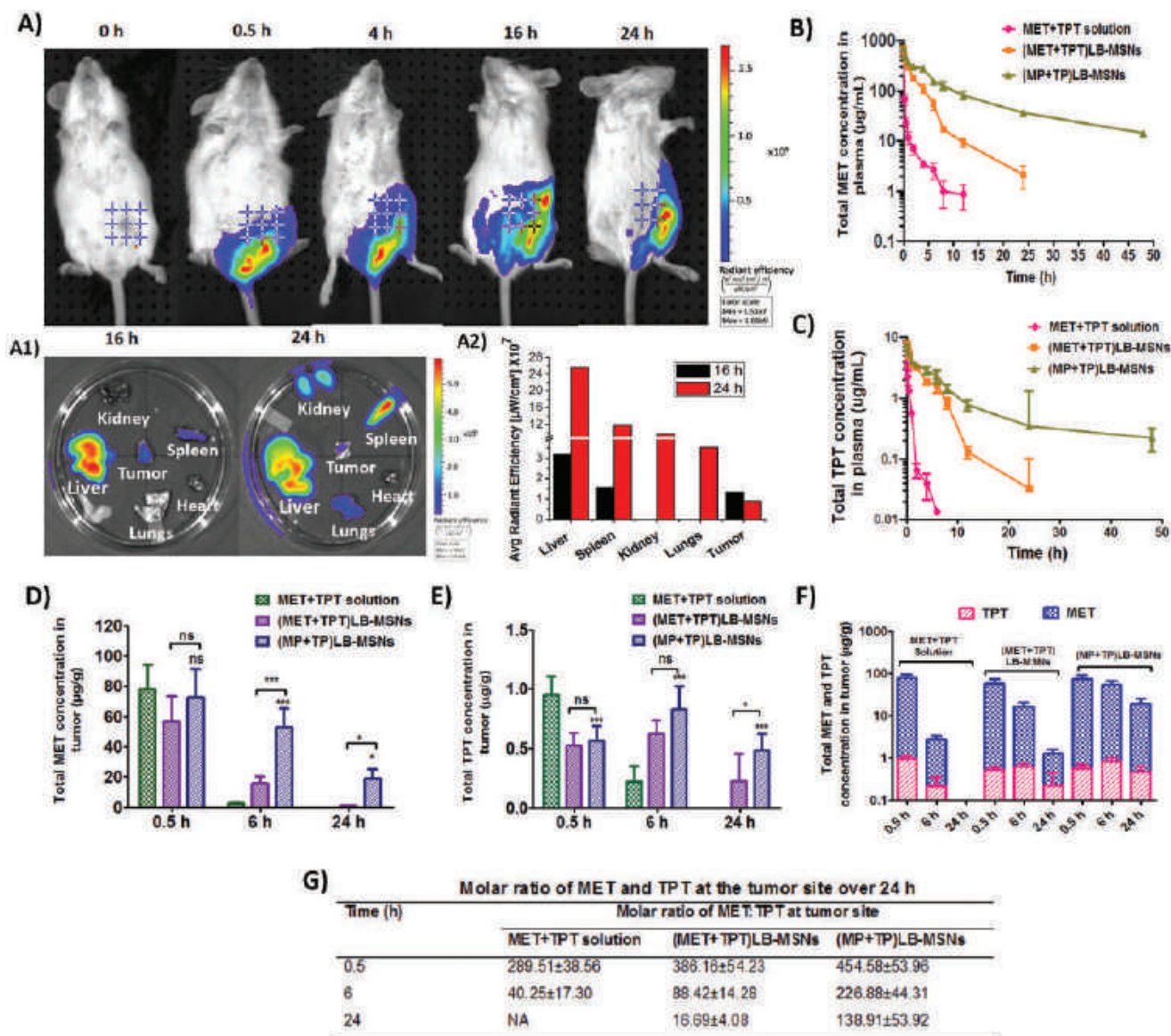


Figure 5. A) Representative IVIS images over 24 h to compare the biodistribution of i.v. injected DiR-labeled LB-MSNs to the 4T1 tumor-bearing mice and A1) ex vivo bioluminescence of explanted organs in the same experiment; animals were sacrificed after 16 h and 24 h. A2) Comparative radiant efficiency in different organs of interest. B,C) MET and TPT concentrations in plasma of different coloaded LB-MSNs with and without trapping agent (MET and TPT were given a dose of 50 and 1 mg kg⁻¹, respectively). D) Total MET concentration, E) total TPT concentration in tumor tissue with respect to time, all data are expressed as mean ± SD ($n = 3$), statistical significance was determined with one-way ANOVA and differences between groups were determined by Tukey's multiple comparison test, * $p \leq 0.05$; ** $p \leq 0.01$; *** $p \leq 0.001$; ns, nonsignificant. F) Comparison of total MET and TPT tumor accumulation between the MET+TPT solution and different LB-MSN formulations. G) Molar ratio of MET and TPT at tumor site as free or LB-MSN formulations.

Table 1. Pharmacokinetic parameters of MET and TPT in mice plasma after single intravenous administration of coloaded MET and TPT formulations at a dosage of 50 mg kg⁻¹ MET and 1 mg kg⁻¹ TPT. Significance level: ****p* ≤ 0.001; ***p* ≤ 0.01; **p* ≤ 0.05; ns, nonsignificant versus MET+TPT solution, all data are expressed as mean ± SD (*n* = 3).

	Metformin (MET)			Topotecan (TPT)		
	MET+TPT solution	(MET+TPT)LB-MSNs	(MP+TP)LB-MSNs	MET+TPT solution	(MET+TPT)LB-MSNs	(MP+TP)LB-MSNs
<i>C</i> _{max} [μg mL ⁻¹]	542.61 ± 17.84	707 ± 25.45	681.76 ± 134.64	3.60 ± 0.028	7.92 ± 0.073	7.74 ± 0.063
<i>t</i> _{1/2} [h]	3.34 ± 1.37	5.84 ± 1.202 ^{ns}	14.42 ± 2.58***	1.76 ± 0.028	2.97 ± 0.11***	10.90 ± 0.733***
AUC ₀₋₄ [μg h mL ⁻¹]	694.8 ± 734.63	1355.66 ± 74.24 ^{ns}	3887.73 ± 340.22***	2.21 ± 0.89	23.120 ± 3.09***	42.063 ± 0.591***
<i>V</i> _{ss} [mL]	155.70 ± 16.5	128.17 ± 14.24	175.59 ± 1.21	6.75 ± 0.19	3.32 ± 0.013	6.25 ± 0.022
Cl [mL h ⁻¹]	158.29 ± 3.5	36.33 ± 2.29***	11.99 ± 1.16***	8.88 ± 0.12	0.859 ± 0.0061***	0.430 ± 0.0038***
MRT [h]	1.92 ± 1.79	3.54 ± 0.61 ^{ns}	14.67 ± 0.87***	0.75 ± 0.04	3.87 ± 0.22***	14.52 ± 0.62***

solution, (MET+TPT)LB-MSNs, and (MP+TP)LB-MSNs through tail vein at an equivalent dose of 50 mg kg⁻¹ MET and 1 mg kg⁻¹ TPT. Plasma distribution profiles over 48 h are shown in Figure 5B,C, and pharmacokinetic parameters are summarized in Table 1. MET+TPT solution eliminated rapidly from the systemic circulation, whereas coloaded MSNs with trapping agent, (MP+TP)LB-MSNs exhibited 2.8-fold, 5.6-fold increase in area under curve (AUC)₀₋₄ of MET and 1.8-fold and 19-fold increase in AUC₀₋₄ of TPT compared to (MET+TPT)LB-MSNs and MET+TPT solution, respectively. The average half-life of (MP+TP)LB-MSNs was 2.4-fold and 4.3-fold longer for MET and 3.6-fold and 6.7-fold longer for TPT compared to the formulation without trapping agent and drug solutions, respectively. These results indicate longer residence of drug in the body by HIP-based coloaded MSNs which further helps in promoting tumor site accumulation by enhanced permeation and retention (EPR) effect. The lower mean residence time (MRT) and half-life of the MET+TPT solution might be attributed to the rapid distribution of the free drug to organs and rapid elimination. Further, a significant difference between the pharmacokinetic parameters of (MP+TP)LB-MSNs and (MET+TPT)LB-MSNs might be due to the faster release of drugs from the MSNs without trapping agent. Increased AUC₀₋₄, MRT, and *t*_{1/2} values of (MP+TP)MSNs claim the controlled release effect of HIP and long circulation due to lipid bilayer coating.

A comparative tumor distribution study was also performed to assess the tumor localization of the formulations. Figure 5D,E compares the MET and TPT concentrations in the tumor at a different time resulting due to various formulations. Apparently, (MP+TP)LB-MSNs delivered more MET and TPT than MET+TPT solution and (MET+TPT)LB-MSNs. To prove the in vivo synergistic efficacy, it is always necessary to deliver the drug ratios exhibiting synergistic cytotoxicity.^[15] To confirm the delivery of synergistic ratio, we have determined the MET:TPT ratio at the tumor site (Figure 5F). The coloaded formulation with trapping agent, (MP+TP)LB-MSNs had maintained molar ratios of MET to TPT at 138.9 to 454.5 at the end of 24 h, which absolutely fall under the region of synergy determined in in vitro synergy modeling experiments. In contrast, MET+TPT solution reached the tumor at synergistic molar ratios in early time points with no detectable limits at 24 h. Further comparison between formulations with and without trapping agent showed low molar ratios of MET to TPT

from (MET+TPT)LB-MSNs, ranging from 16 to 386, clearly demonstrating that HIP-based controlled release of MET and TPT helps in maintaining high tumor site concentrations for a prolonged period of time (Figure 5G).

2.3.3. In Vivo Tumor Regression Studies

After having superior in vitro activity and improved pharmacokinetics, various LB-MSNs were tested for in vivo efficacy in BALB/c mice bearing 4T1 mammary tumors and compared with free MET, TPT, and control. Treatment was started when the tumor volume reached ≈100 mm³ in all the animals. Each group received i.v. dose of MET and TPT equivalent to 50 and 1 mg kg⁻¹, respectively, on days 1, 4, 8, 12, and 16. The tumor volume versus time curve and tumor photographs are presented in Figure 6A,D. Tumor volume was measured throughout the study, and animals were sacrificed on the 20th day of the study started, to harvest the tumors and organs. As shown in Figure 6A, for single drug formulations, both (MP)LB-MSNs and (TP)LB-MSNs had slightly better antitumor activity than the corresponding drug solutions, but no significant difference was observed (*p* > 0.05). For combination formulations, the tumor growth was better inhibited than single drug-loaded formulations. The mixture of solutions (MET+TPT solution) and a mixture of single drug loaded MSNs (MP)LB-MSNs+(TP)LB-MSNs had similar effects. Coloaded (MP+TP)LB-MSNs showed superior antitumor activity than their solutions and the mixture of single drug loaded LB-MSNs with significant differences (*p* ≤ 0.05). The final tumor volume at the end of 20 days post-treatment of coloaded (MP+TP)LB-MSNs treated group was 13.9-fold, 4.06-fold, and 1.84-fold lower than control, free MET+TPT, and mixture (MP)LB-MSN+(TP) LB-MSN-treated groups, respectively. Whereas, mixture of LB-MSNs had shown 7.5-fold and 2.20-fold lower tumor volumes compared to control and free MET+TPT groups, respectively. The final tumor weight of coloaded formulation at the end of tumor regression study was 32-fold, 9.69-fold, and 2.29-fold lower than the control group, MET+TPT solution, and mixture(MP)LB-MSN+(TP)LB-MSN group (*p* < 0.001) (Figure 6B). The body weight of mice was also recorded to evaluate the safety of the formulations. As seen in Figure 6C, TPT solution and (TP)LB-MSNs showed

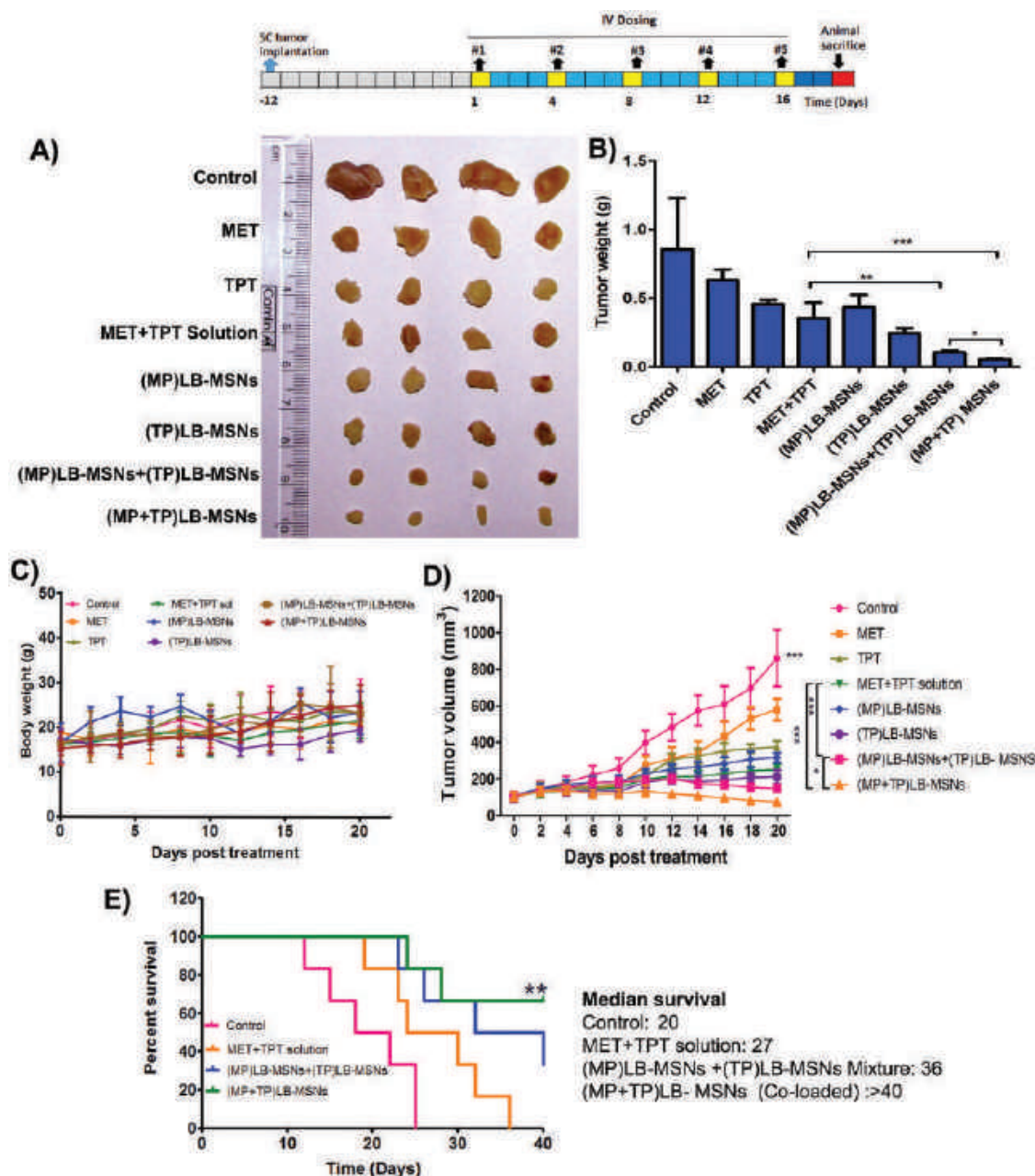


Figure 6. In vivo antitumor activity against 4T1 cells transplanted mammary tumor in female BALB/c mice (MET dose: 50 mg kg⁻¹ and TPT dose: 1 mg kg⁻¹ body weight). A) Morphology of the tumors harvested at the end of the study. B) Tumor volume versus time at different time points of the study. All data are expressed as mean \pm SD ($n = 6$), statistical significance was determined with one-way ANOVA analysis. Differences between groups were determined by a Tukey's multiple comparison test, $*p \leq 0.05$; $**p \leq 0.01$; $***p \leq 0.001$; ns, nonsignificant. C) Body weight changes during the study period. D) Survival rates of 4T1 tumor-bearing mice administrated with a MET+TPT solution and MET+TPT-loaded LB-MSNs, survival data were generated by the Kaplan–Meier method, median survival and statistical significance were determined by log-rank test and Mann–Whitney U test, respectively ($n = 6$), $**p \leq 0.01$.

comparative weight loss than free MET and its combination treatment arms MET+TPT solution, (MP)LB-MSNs+(TP) LB-MSNs, and coloaded (MP+TP)LB-MSNs, indicating that MET increasing the safety profile of the TPT. The better tumor inhibition efficacy of coloaded formulations can be attributed to better pharmacokinetic profile and controlled drug delivery with the ratiometric synergistic combinatorial delivery of MET and TPT which resulted in higher residence

time in body compared to free drug solution that was getting rapidly eliminating from the body.

2.3.4. Survival Analysis

The survival studies were performed for 40 days after the treatment started, and it was found that survival rates

increased significantly on the administration of coloaded LB-MSNs in comparison to the MET+TPT solution and mixture LB-MSNs. The median survival times for mice treated with saline, MET+TPT solution, mixture of (MP)LB-MSNs+(TP) LB-MSNs, and coloaded (MP+TP)LB-MSNs were 20, 27, 36, and >40 days, respectively (Figure 6E). Treatment with MET+TPT solution and mixture LB-MSNs showed slightly improved survival profiles, whereas coloaded (MP+TP)LB-MSNs enhanced median survival time more than 40 days ($p \leq 0.01$).

3. Conclusion

In this study, we successfully developed a novel in situ HIP-based active loading technique for the efficient loading and controlled release of MET and TPT using pseudo-cell-like LB-MSNs as templates. The developed delivery system was able to control the release of MET and TPT. This resulted in significantly increased intracellular concentrations of MET which is a major translational concern in the MET therapy in cancer. By rational design of these LB-coated MSNs with the synergistic ratio of intended drugs identified by synergy modeling provides deterministic delivery of drug inside the tumor cells. Co-loaded MET and TPT formulations demonstrated higher in vitro cytotoxicity and related apoptotic effects compared to the mixture of single drugs and drug-loaded MSNs. The enhanced tumor efficacy was consistent with the in vitro cell cycle and apoptotic effects. All these presented results prove that translational challenges of MET could be successfully addressed by rational design of the high payload bearing MSNs with controlled release profile. Since the safety and clinical benefits are already proven with other chemotherapeutic agents, therapies could be designed by appropriate selection and delivery of the synergistic ratios at the tumor site. To the best of our knowledge, the present reported active loading procedure using LB-MSNs is the first of its kind and this could be a novel platform technology for the ionic drugs which are difficult to load by using conventional active loading techniques.

4. Experimental Section

Materials: MET was procured from Sigma-Aldrich (St. Louis, MO, USA), TPT HCl was received as a gift sample from Dabur Pharmaceuticals Pvt. Ltd. DSPE-PEG₂₀₀₀, soya phosphatidylcholine, cholesterol, cetyltrimethylammonium bromide (CTAB), Pluronic F-127 were purchased from Sigma-Aldrich (St. Louis, MO, USA). Tetraethylorthosilicate (TEOS), and pamoic acid disodium salt were purchased from TCI chemicals, India Pvt. Ltd. Cell culture media and supplements were purchased from Invitrogen (Carlsbad, CA). MTT, FITC, PI, and RNase were purchased from Sigma-Aldrich (St. Louis, MO, USA). High performance liquid chromatography (HPLC) solvents such as acetonitrile and methanol were purchased from Merck (India). All other chemical reagents were of analytical, cell culture grade and obtained from commercial sources. Triple-distilled water (TDW) was prepared from Milli Q system (Millipore, Bedford, MA, USA).

Identification of Synergy between MET and TPT: Before formulation development, the synergy between MET and TPT was screened by using regular cytotoxicity assay (MTT assay). To identify the synergy

combinations, 6×6 checkerboard format was used, and results were evaluated using COMBENEFIT software package. The detailed procedure of MTT assay and modeling is discussed in cell culture section provided in the Supporting Information.

Selection of APIs and Counterion for HIP Formation: Based on the acid dissociation constants (pK_a) of MET, 12.4, and TPT, 8 and 9.83, PA was evaluated as the counterion for the HIP formation. The detailed procedure of HIP synthesis and evaluation is provided in the Supporting Information.

Preparation of LB-MSNs and Drug Loading by Using the HIP Approach—Loading of Pamoic Acid into MSNs and Lipid Bilayer Coating (PA)LB MSNs: Typical MSN cores were prepared by well-reported Stöbers process^[33] (see the Supporting Information for detailed procedure). PA-loaded MSN cores were prepared by passive adsorption process. Briefly, 100 mg of plain MSNs were soaked in 5 mL of aqueous 10×10^{-3} M solution of PA (disodium salt) followed by probe sonication for 2 min with a power output of 20 W. After sonication, MSN suspension was incubated in the same solution for 12 h. The PA-loaded particles were then coated with a lipid film obtained by solvent evaporation of a mixture of 25 mg of SoyPC/Chol/DSPE-PEG₂₀₀₀ (molar ratio 7:2.75:0.25) dissolved in chloroform to a 25 mL round bottom flask under rotary evaporation. For uniform coating of the lipid film, probe sonication was used for 10 min with intermittent on/off cycles at a power output of 25 W. Untrapped PA was removed by centrifugation at 12 000 rpm for 15 min.

Preparation of LB-MSNs and Drug Loading by Using the HIP Approach—Use of (PA)LB MSNs for Remote Loading of MET and TPT: Different conditions were used for the active loading of MET and TPT. MET at a concentration of 10 mg mL^{-1} was dissolved in phosphate buffered sucrose (10% w/v sucrose and phosphate buffered saline (PBS) pH 9), which was mixed with (PA)LB-MSNs to achieve a MET/MSN weight ratio of 1:1. Similarly, TPT at 1 mg mL^{-1} was dissolved in PBS and was mixed with (PA)LB-MSNs to achieve TPT/MSN ratio of 1:2. After that, the mixture was incubated for 4 h at 60 °C under constant shaking. Similar conditions were followed for coloaded of both MET and TPT. The ratio of MET and TPT was adjusted based on the percent of entrapment of individual drugs. After incubation, drug-loaded particles were centrifuged at 10 000 rpm for 15 min, and the supernatant was removed and replaced with 10% sucrose for the lyophilization. Lyophilization was carried out at -55 °C for 24 h under 0.1 bar vacuum. For comparative evaluation, formulations without trapping agent were prepared using passive adsorption process and the rest of the procedure was same.

Preparation of LB-MSNs and Drug Loading by Using the HIP Approach—Physicochemical Characterization of LB-MSNs: All developed formulations were evaluated for particle size, zeta potential, drug loading efficiency, in vitro drug release profiles, and confirmation of in situ HIP formation. Apart from that, various parameters that affect the drug loading conditions like, pH, type of gradient ion, and temperature were also evaluated. To confirm the membrane permeability of metformin, in vitro permeability assay was also performed. Detailed methods are described in the Supporting Information.

Preparation of LB-MSNs and Drug Loading by Using the HIP Approach—In Vitro Cell-Based Assays: To evaluate the efficiency of developed formulation, cell-based assays were performed in MDA-MB-231 and 4T1 (human and mouse, respectively) breast cancer cell lines by following established experimental protocols. Cytotoxicity assays and synergy calculations were performed by modeling approach using COMBENEFIT software package in 6×6 checkerboard format. Other cell-based assays like cell cycle arrest, apoptosis, mitochondrial membrane potential, cell uptake studies were performed as per the manufacturer and reported experimental protocols. A detailed description of experimental procedures and conditions is provided in the Supporting Information.

Preparation of LB-MSNs and Drug Loading by Using the HIP Approach—In Vivo Studies: All the animals for in vivo experiments were procured from the National Laboratory Animal Center (NLAC) CDRI and acclimatized for 1 week. All the protocols for animal experiments were

approved by the Institutional Animal Ethical Committee CSIR-CDRI (approval no: IAEC/2016/159).

Preparation of LB-MSNs and Drug Loading by Using the HIP Approach—Tumor Model Development: Subcutaneous murine breast cancer model was used for the evaluation of the developed formulations. The breast cancer model was developed in 6–8 week old female BALB/c mice weighing 20–22 g using murine mammary carcinoma cells, 4T1. Cells at a density of 1×10^6 were injected subcutaneously at the mammary gland near to lower right quadrant of the abdomen of mice. In vivo NIRF imaging, pharmacokinetics, and tumor distribution studies were carried out in mice with a tumor volume ranging 200–300 mm³, whereas tumor regression study and survival analysis were performed in mice with 100 mm³ tumor volume.

Preparation of LB-MSNs and Drug Loading by Using the HIP Approach—In Vivo NIRF Imaging: In order to observe the biodistribution of the LB-MSNs intuitively, real-time NIRF imaging was applied to monitor the fate of the LB-MSNs in vivo. DiR, a NIRF dye, was selected as an indicator and MSNs were prepared by passive loading approach similar to the procedure followed for the preparation of dye-loaded MSNs in cell uptake studies. 150 μ L of (DiR)LB-MSNs containing DiR dose of 1 mg kg⁻¹ was injected intravenously via tail vein to 4T1 tumor-bearing female BALB/c mice. After 0.5, 4, 16, and 24 h, mice were anesthetized with 2% isoflurane and placed on their back into a light-tight chamber. At the end of the imaging, the mice were sacrificed and heart, liver, spleen, lung, kidney, and tumor were harvested for ex vivo imaging. The real-time NIRF images were taken using Xenogen IVIS Lumina system (Caliper Life Sciences, USA) with the indocyanine green (ICG) filter (excitation at 745 nm, emission at 835 nm) at time points. The exposure time was set to 3 s. Results were analyzed using Living Image 3.1 software (Caliper Life Sciences, USA).

Preparation of LB-MSNs and Drug Loading by Using the HIP Approach—Pharmacokinetics and Tumor Distribution of MET and TPT from Various Formulations: In order to evaluate the in vivo codelivery of MET and TPT MSNs and the effect of ion trapping agent on the release and distribution, 4T1 tumor-bearing female BALB/c mice were used and they were compared with plain drugs. When tumor volume reached 200–300 mm³, mice were assigned into 3 groups, 1) free MET+TPT solution, 2) coloaded (MET+TPT)LB-MSNs, without trapping agent, 3) coloaded (MP+TP)LB-MSNs, with trapping agent containing MET and TPT equivalent to 50 and 1 mg kg⁻¹, respectively. At designated time points, mice were anesthetized, blood was collected, plasma separated by centrifugation, and stored at -20 °C until analysis. Tumors were collected and frozen immediately and stored at -80 °C. After extraction from the biological samples, MET and TPT were analyzed by HPLC method as described and plasma concentration–time profiles were fitted to the noncompartmental analysis using Phoenix software package.

Preparation of LB-MSNs and Drug Loading by Using the HIP Approach—In Vivo Antitumor Efficacy: In vivo antitumor efficacy of the MET- and TPT-loaded MSNs was evaluated in 4T1 cells bearing mouse model. When the tumor size reached ≈ 100 mm³, mice were randomly divided into eight groups ($n = 5$) and administered through i.v. route with saline, MET solution, TPT solution, MET+TPT solution, (MP)LB-MSNs, (TP)LB-MSNs, (MP)LB-MSN+(TP)LB-MSN mixture, and coloaded (MP+TP)MSNs, respectively, through tail vein on days 0, 4, 8, 12, and 16. The dosage of MET or TPT was kept at 50 and 1 mg kg⁻¹, respectively. Tumor volumes were measured throughout the experiment and calculated according to the formula: $(L \times W^2)/2$, in which L is the longest and W is the shortest tumor diameter (mm). Mice were sacrificed, and tumors were harvested at the completion of the experiment. Changes in body weights were also measured regularly as the indicator of general toxicity. After completion of experiment tumors was excised, tumor weights were measured and tissues were collected for histology.^[27a]

Preparation of LB-MSNs and Drug Loading by Using the HIP Approach—Survival Analysis: In a separate experiment similar to the tumor regression study, 4T1 tumor-bearing mice were divided into four groups with six animals in each group (control, MET+TPT solution, (MP)LB-MSN+(TP)LB-MSN mixture, and coloaded (MP+TP)LB-MSNs

and treatment was started after reaching the tumor volume 100 mm³. Animals were treated as per the protocol described above in the tumor regression study. However, survival study was conducted up to 40 days after the treatment started and end point of survival was defined as animal death or when implanted tumor volume reaches ≈ 1000 mm³.

Preparation of LB-MSNs and Drug Loading by Using the HIP Approach—Statistical Analysis: Cell viability and synergy calculations were calculated using three biological replicates. Cell viability and cell growth were normalized to the negative control (untreated cells that receive saline). Synergy calculations and statistical significance were determined using COMBENEFIT software.

In pharmacokinetic studies, statistical significance of tumor distribution data was determined by using one way analysis of variance (ANOVA) in Graphpad prism (GraphPad 5.0 Software, Inc., La Jolla, CA, USA). All data were expressed as mean \pm standard deviation (SD) ($n = 3$). Differences between groups were determined by Tukey's multiple comparison test. Asterisks denote statistically significant differences (* $p < 0.05$; ** $p < 0.01$; *** $p < 0.001$).

In in vivo tumor regression studies, statistical significance of tumor volume and tumor weight were evaluated by using one way ANOVA in Graphpad prism (GraphPad 5.0 Software, Inc., La Jolla, CA, USA). All data were expressed as mean \pm standard deviation ($n = 6$). Differences between groups were determined by Tukey's multiple comparison test. Asterisks denote statistically significant differences (* $p < 0.05$; ** $p < 0.01$; *** $p < 0.001$).

Survival data were generated by the Kaplan–Meier method, median survival and statistical significance were determined by log-rank test and Mann–Whitney U test, respectively. All data were expressed as mean \pm standard deviation ($n = 6$). The statistical analysis of data was carried out using Graph pad prism 5.0 software (GraphPad PRISM, San Diego, CA, USA). Asterisks denote statistically significant differences (* $p < 0.05$; ** $p < 0.01$; *** $p < 0.001$).

Supporting Information

Supporting information is available from the Wiley online library or from the author.

Acknowledgements

The authors would like to thank CSIR, New Delhi for providing research fellowship and the CSIR-CDRI for research facilities. The authors also would like to thank A. L. Vishwakarma and Madhu Chaturvedi for assisting with flow cytometry experiments. And, Dr. Kavita Singh is thankfully acknowledged for contribution in the CLSM facility of Electron microscopy Division. The authors are thankful to the DBT India, for funding through Grant No. GAP0220 and the CSIR-CDRI for funding through Grant No. ESC0103. CDRI communication number for this manuscript was 9724.

Conflict of Interest

The authors declare no conflict of interest.

Keywords

breast cancer, codelivery, ion pairing, mesoporous silica nanoparticles, synergy

Received: March 23, 2018

Revised: July 17, 2018

Published online:

- [1] a) A. Kreso, C. A. O'Brien, P. van Galen, O. I. Gan, F. Notta, A. M. Brown, K. Ng, J. Ma, E. Wienholds, C. Dunant, A. Pollett, S. Gallinger, J. McPherson, C. G. Mullighan, D. Shibata, J. E. Dick, *Science* **2013**, 339, 543; b) R. X. Zhang, H. L. Wong, H. Y. Xue, J. Y. Eoh, X. Y. Wu, *J. Controlled Release* **2016**, 240, 489.
- [2] a) C. E. Ashley, E. C. Carnes, G. K. Phillips, D. Padilla, P. N. Durfee, P. A. Brown, T. N. Hanna, J. Liu, B. Phillips, M. B. Carter, N. J. Carroll, X. Jiang, D. R. Dunphy, C. L. Willman, D. N. Petsev, D. G. Evans, A. N. Parikh, B. Chackerian, W. Wharton, D. S. Peabody, C. J. Brinker, *Nat. Mater.* **2011**, 10, 389; b) Y. Chen, H. Chen, J. Shi, *Mol. Pharmaceutics* **2014**, 11, 2495.
- [3] a) A. Makkouk, G. J. Weiner, *Cancer Res.* **2015**, 75, 5; b) T. Yin, L. Wang, L. Yin, J. Zhou, M. Huo, *Biomaterials* **2015**, 61, 10; c) K. M. Au, Y. Min, X. Tian, L. Zhang, V. Perello, J. M. Caster, A. Z. Wang, *ACS Nano* **2015**, 9, 8976.
- [4] a) L. M. Phan, S.-C. J. Yeung, M.-H. Lee, *Cancer Biol. Med.* **2014**, 11, 1; b) D. Hanahan, R. A. Weinberg, *Cell* **2011**, 144, 646; c) G. J. Yoshida, *J. Exp. Clin. Cancer Res.* **2015**, 34, 111; d) M. A. Pierotti, F. Berrino, M. Gariboldi, C. Melani, A. Mogavero, T. Negri, P. Pisanis, S. Pilotti, *Oncogene* **2013**, 32, 1475.
- [5] a) Y. K. Chae, A. Arya, M.-K. Malecek, D. S. Shin, B. Carneiro, S. Chandra, J. Kaplan, A. Kalyan, J. K. Altman, L. Platanias, F. Giles, *Oncotarget* **2016**, 7, 40767; b) I. N. Alimova, B. Liu, Z. Fan, S. M. Edgerton, T. Dillon, S. E. Lind, A. D. Thor, *Cell Cycle* **2009**, 8, 909; c) A. Sonnenblick, D. Agbor-Tarh, I. Bradbury, S. Di Cosimo, H. A. Azim, D. Fumagalli, S. Sarp, A. C. Wolff, M. Andersson, J. Kroep, T. Cufer, S. D. Simon, P. Salman, M. Toi, L. Harris, J. Gralow, M. Keane, A. Moreno-Aspitia, M. Piccart-Gebhart, E. de Azambuja, *J. Clin. Oncol.* **2017**, 35, 1421.
- [6] G. Zhou, R. Myers, Y. Li, Y. Chen, X. Shen, J. Fenyk-Melody, M. Wu, J. Ventre, T. Doebber, N. Fujii, N. Musi, M. F. Hirshman, L. J. Goodyear, D. E. Moller, *J. Clin. Invest.* **2001**, 108, 1167.
- [7] a) D. R. Morales, A. D. Morris, *Annu. Rev. Med.* **2015**, 66, 17; b) R. Ramjeesingh, C. Orr, C. S. Bricks, W. M. Hopman, N. Hamad, *Curr. Oncol.* **2016**, 23, e116.
- [8] R. J. Dowling, S. Niraula, V. Stambolic, P. J. Goodwin, *J. Mol. Endocrinol.* **2012**, 48, 12.
- [9] M. Peng, K. O. Darko, T. Tao, Y. Huang, Q. Su, C. He, T. Yin, Z. Liu, X. Yang, *Cancer Treat. Rev.* **2017**, 54, 24.
- [10] a) T. Hu, Y. M. Chung, M. Guan, M. Ma, J. Ma, J. S. Berek, M. C. T. Hu, *Sci. Rep.* **2014**, 4, 5810; b) <https://clinicaltrials.gov/ct2/show/NCT01528046>, (accessed: March 2018).
- [11] J. von Pawel, U. Gatzemeier, J. L. Pujol, L. Moreau, S. Bildat, M. Ranson, G. Richardson, C. Steppert, A. Riviere, I. Camlett, S. Lane, G. Ross, *J. Clin. Oncol.* **2001**, 19, 1743.
- [12] M. Rodriguez, P. G. Rose, *Gynecol. Oncol.* **2001**, 83, 257.
- [13] C. Oberhoff, D. G. Kieback, R. Wurstein, H. Deertz, J. Sehouli, C. van Soest, J. Hilfrich, M. Mesrogli, G. von Minckwitz, H. J. Staab, A. E. Schindler, *Onkologie* **2001**, 24, 256.
- [14] A. Korfel, C. Oehm, J. von Pawel, U. Keppler, M. Deppermann, S. Kaubitsch, E. Thiel, *Eur. J. Cancer* **2002**, 38, 1724.
- [15] a) L. D. Mayer, T. O. Harasym, P. G. Tardi, N. L. Harasym, C. R. Shew, S. A. Johnstone, E. C. Ramsay, M. B. Bally, A. S. Janoff, *Mol. Cancer Ther.* **2006**, 5, 1854; b) J. H. Lee, A. Nan, *J. Drug Delivery* **2012**, 2012, 17; c) R. X. Zhang, P. Cai, T. Zhang, K. Chen, J. Li, J. Cheng, K. S. Pang, H. A. Adissu, A. M. Rauth, X. Y. Wu, *Nanomedicine* **2016**, 12, 1279.
- [16] a) F. Z. Dahmani, Y. Xiao, J. Zhang, Y. Yu, J. Zhou, J. Yao, *Adv. Healthcare Mater.* **2016**, 5, 1447; b) D. Chen, Q. Tang, J. Zou, X. Yang, W. Huang, Q. Zhang, J. Shao, X. Dong, *Adv. Healthcare Mater.* **2018**, 15, 201701272.
- [17] B. Zhang, T. Wang, S. Yang, Y. Xiao, Y. Song, N. Zhang, S. Garg, *J. Controlled Release* **2016**, 238, 10.
- [18] S. Gadde, *MedChemComm* **2015**, 6, 1916.
- [19] Y. H. Song, E. Shin, H. Wang, J. Nolan, S. Low, D. Parsons, S. Zale, S. Ashton, M. Ashford, M. Ali, D. Thrasher, N. Boylan, G. Troiano, *J. Controlled Release* **2016**, 229, 106.
- [20] Z. Li, J. C. Barnes, A. Bosoy, J. F. Stoddart, J. I. Zink, *Chem. Soc. Rev.* **2012**, 41, 2590.
- [21] a) J. L. Vivero-Escoto, I. I. Slowing, B. G. Trewyn, V. S. Y. Lin, *Small* **2010**, 6, 1952; b) H. Zhang, D. R. Dunphy, X. Jiang, H. Meng, B. Sun, D. Tarn, M. Xue, X. Wang, S. Lin, Z. Ji, R. Li, F. L. Garcia, J. Yang, M. L. Kirk, T. Xia, J. I. Zink, A. Nel, C. J. Brinker, *J. Am. Chem. Soc.* **2012**, 134, 15790.
- [22] a) K. S. Butler, P. N. Durfee, C. Theron, C. E. Ashley, E. C. Carnes, C. J. Brinker, *Small* **2016**, 12, 2173; b) Y. He, Z. Su, L. Xue, H. Xu, C. Zhang, *J. Controlled Release* **2016**, 229, 80; c) W.-H. Chen, G.-F. Luo, Q. Lei, F.-Y. Cao, J.-X. Fan, W.-X. Qiu, H.-Z. Jia, S. Hong, F. Fang, X. Zeng, R.-X. Zhuo, X.-Z. Zhang, *Biomaterials* **2016**, 76, 87; d) Y. Chen, K. Ai, J. Liu, G. Sun, Q. Yin, L. Lu, *Biomaterials* **2015**, 60, 111; e) X. Wu, Z. Wang, D. Zhu, S. Zong, L. Yang, Y. Zhong, Y. Cui, *ACS Appl. Mater. Interfaces* **2013**, 5, 10895; f) P. N. Durfee, Y.-S. Lin, D. R. Dunphy, A. J. Muñiz, K. S. Butler, K. R. Humphrey, A. J. Lokke, J. O. Agola, S. S. Chou, I. M. Chen, W. Wharton, J. L. Townson, C. L. Willman, C. J. Brinker, *ACS Nano* **2016**, 10, 8325; g) V. Cauda, H. Engelke, A. Sauer, D. Arcizet, C. Bräuchle, J. Rädler, T. Bein, *Nano Lett.* **2010**, 10, 2484.
- [23] Q. Yang, T. Zhang, C. Wang, J. Jiao, J. Li, Y. Deng, *Eur. J. Pharm. Biopharm.* **2014**, 88, 737.
- [24] H. Yu, Q. Wang, Y. Sun, M. Shen, H. Li, Y. Duan, *PLoS One* **2015**, 10, e0116502.
- [25] X. Liu, A. Situ, Y. Kang, K. R. Villabroza, Y. Liao, C. H. Chang, T. Donahue, A. E. Nel, H. Meng, *ACS Nano* **2016**, 10, 2702.
- [26] H. Meng, M. Wang, H. Liu, X. Liu, A. Situ, B. Wu, Z. Ji, C. H. Chang, A. E. Nel, *ACS Nano* **2015**, 9, 3540.
- [27] a) A. Verma, S. Sharma, P. K. Gupta, A. Singh, B. V. Teja, P. Dwivedi, G. K. Gupta, R. Trivedi, P. R. Mishra, *Acta Biomater.* **2016**, 31, 288; b) S. B. Koh, A. Courtin, R. J. Boyce, R. G. Boyle, F. M. Richards, D. I. Jodrell, *Cancer Res.* **2015**, 75, 3583.
- [28] a) D. M. Jonker, S. A. Visser, P. H. van der Graaf, R. A. Voskuyl, M. Danhof, *Pharmacol. Ther.* **2005**, 106, 1; b) J. B. Fitzgerald, B. Schoeberl, U. B. Nielsen, P. K. Sorger, *Nat. Chem. Biol.* **2006**, 2, 458.
- [29] M. Jurkiewicz, D. A. Averill-Bates, M. Marion, F. Denizeau, *Biochim. Biophys. Acta, Mol. Cell Res.* **2004**, 1693, 15.
- [30] Y. Feng, C. Ke, Q. Tang, H. Dong, X. Zheng, W. Lin, J. Ke, J. Huang, S. C. Yeung, H. Zhang, *Cell Death Dis.* **2014**, 5, e1088.
- [31] Y. Yu, Z.-H. Wang, L. Zhang, H.-J. Yao, Y. Zhang, R.-J. Li, R.-J. Ju, X.-X. Wang, J. Zhou, N. Li, W.-L. Lu, *Biomaterials* **2012**, 33, 1808.
- [32] X. Cai, X. Hu, X. Tan, W. Cheng, Q. Wang, X. Chen, Y. Guan, C. Chen, X. Jing, *PLoS One* **2015**, 10, e0133349.
- [33] T.-W. Kim, P.-W. Chung, V. S. Y. Lin, *Chem. Mater.* **2010**, 22, 5093.

Anisamide-Anchored Lyotropic Nano-Liquid Crystalline Particles with AIE Effect: A Smart Optical Beacon for Tumor Imaging and Therapy

Sandeep Urandur,[†] Venkatesh Teja Banala,[†] Ravi Prakash Shukla,[†] Naresh Mittapelly,[†] Gitu Pandey,[†] Navodayam Kalleti,[‡] Kalyan Mitra,[§] Srikanta Kumar Rath,[‡] Ritu Trivedi,^{||} Pratibha Ramarao,[⊥] and Prabhat Ranjan Mishra^{*,†}

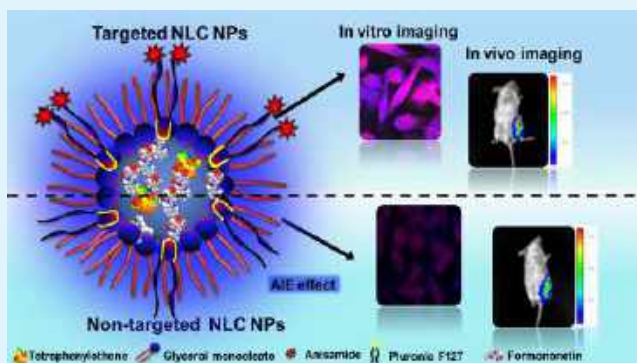
[†]Division of Pharmaceutics, [‡]Division of Toxicology, [§]Electron Microscopy Division, and ^{||}Division of Endocrinology, CSIR-Central Drug Research Institute, Lucknow 226031, India

[⊥]Soft Condensed Matter Lab, Raman Research Institute, Bangalore 560080, India

Supporting Information

ABSTRACT: The prospective design of nanocarriers for personalized oncotherapy should be an ensemble of targeting, imaging, and noninvasive therapeutic capabilities. Herein, we report the development of the inverse hexagonal nano-liquid crystalline (NLC) particles that are able to host formononetin (FMN), a phytoestrogen with known anticancer activity, and tetraphenylethene (TPE), an iconic optical beacon with aggregation-induced emission (AIE) signature, simultaneously. Ordered three-dimensional mesoporous internal structure and high-lipid-volume fraction of NLC nanoparticles (NLC NPs) frame the outer compartment for the better settlement of payloads. Embellishment of these nanoparticles by anisamide (AA), a novel sigma receptor targeting ligand using carbodiimide coupling chemistry ensured NLC's as an outstanding vehicle for possible utility in surveillance of tumor location as well as the FMN delivery through active AIE imaging. The size and structural integrity of nanoparticles were evaluated by quasi-elastic light scattering, cryo field emission scanning electron microscopy small-angle X-ray scattering. The existence of AIE effect in the nanoparticles was evidenced through the photophysical studies that advocate the application of NLC NPs in fluorescence-based bioimaging. Moreover, confocal microscopy illustrated the single living cell imaging ability endowed by the NLC NPs. In vitro and in vivo studies supported the enhanced efficacy of targeted nanoparticles (AA-NLC-TF) in comparison to nontargeted nanoparticles (NLC-TF) and free drug. Apparently, this critically designed multimodal NLC NPs may establish a promising platform for targeted and image-guided chemotherapy for breast cancer.

KEYWORDS: liquid crystals, formononetin, aggregation-induced emission, optical imaging, sigma receptors



1. INTRODUCTION

The development of multifunctional nanoparticles for synchronized imaging and tumor-targeted noninvasive therapy through optical imaging is supposed to have a notable impact on future personalized oncology. Routine X-ray mammography to detect breast cancer involves exposure to harmful ionizing radiation and experiences poor diagnostic accuracy, resulting in a high rate of false-positive diagnosis.^{1–3} In contrast, emerging optical fluorescence imaging modality is safe, inexpensive, accurate, and detect cancer at a primitive stage long before the phenotypic changes occur with excellent spatial resolution.⁴ Among various contrast agents employed for bioimaging, optical beacons with distinct aggregation-induced emission (AIE) property has been gaining importance nowadays and outperforms the flaws of inorganic contrast agents like small Stokes shift, low photostability, low molar absorptivity and

heavy metal cytotoxicity.^{5,6} Thus, AIE fluorogens opened a new avenue in the development of stable and cytocompatible fluorescent probes for long-term noninvasive bioimaging application.^{7,8} Nanomaterials with a combination of diagnostic and therapeutic functions into one theranostics systems are prominent these days and form an all-in-one approach.

Currently, lyotropic nano-liquid crystalline (NLC) phase particles are emerging as an attractive carrier system due to its ability to carry hydrophobic, hydrophilic as well as amphiphilic drugs.^{9–11} Its peculiar high lipid volume fraction and ordered three-dimensional (3D) mesoporous internal structure, provides the greater stability and controlled release of the lipophilic

Received: December 16, 2017

Accepted: March 26, 2018

Published: March 26, 2018

cargos compared to conventional liposomes, this attribute has made NLCs as a potential alternative delivery vehicle for pharmaceuticals.^{12–14} Here we focus on inverse hexagonal (HII) phase liquid crystals for the development of multimodal nanoparticles ensemble of tumor-targeting, imaging and therapeutic properties simultaneously. We have designed a novel sigma receptor ligand, anisamide (AA)-grafted Pluronic F127 (PF127), using carbodiimide chemistry for the stabilization of glyceryl monooleate (GMO)-based nanoparticles (NLC NPs). Further, the AIE effect was imparted using tetraphenylethene (TPE), an iconic fluorogen in combination with a phytoestrogen, formononetin (FMN), for its spatiotemporal release.

TPE is a propeller-shaped molecule, which, in the dissolved state, possesses torsional motions capable of relaxing the energy of absorbed photons nonradiatively, whereas on aggregation, they promote efficient photoluminescence due to the restriction of their intramolecular rotations (RIR).^{15,16} Although TPE has absorption maxima, emission spectra are located below the near-infrared (NIR) region. It was used to show that TPE has advantage over conventional organic dyes, which are highly emissive when dissolved, but once clustered in the nanoparticles, aggregation-caused quenching (ACQ) of fluorescence limits the doping amount of dyes, which cannot be swapped by simply increasing the amount of dye concentration. However, there are several reports, where, by modifying TPE with strong electron-donating groups or extending the conjugation length of the π -system, it shows increase in transient absorption in the NIR region (bathochromic shift).^{17,18} Moreover, the major factor for the development of bioprobe for in vivo bioimaging is biocompatibility of the imaging agents. Other AIE system like anthracene derivatives are carcinogenic, and AIEgen metal complexes pose a daunting obstacle due to their intrinsic cytotoxicity.^{19,20} Besides, the unique property to overcome the ACQ effect of conventional organic fluorophores, safety profile along with high “off–on” contrast ratio, large Stokes-shifted fluorescence, long luminescence lifetime, strong photobleaching resistance, and simple and cheap chemical synthesis of TPE-based materials have driven us to select TPE over other AIEgens.^{21–23}

Embellishment of drug-delivery vehicle by AA like small molecular ligand enhances the tumor detection with high specificity.^{24,25} They locate the overexpressed sigma receptors on breast cancer cells, and then the loaded smart optical beacon reports the cancer location by the way of fluorescent glow.²⁶ FMN (7-hydroxy-40-methoxyisoflavone) is a phytoestrogenic isoflavone proven to induce apoptosis, which inhibits cell proliferation and cell cycle progression in breast cancer, prostate cancer, and cervical cancer. Moreover, it possesses immunomodulatory, cardioprotective, and hypolipidemic activities.^{27,28} Despite its prodigious biological outcomes, FMN bioactivity is highly limited due to low aqueous solubility (0.05 mg/mL) and extensive metabolism by glucuronidation and sulfation, which altogether attributed to its low systemic or target site concentrations and confined the clinical application.^{29–31} It is thus envisaged to fabricate a stable, effective, and safe delivery system to circumvent the poor solubility and its collateral effects of FMN.

Throughout this article, it was shown that inverse hexagonal NLC NPs co-loaded with AIE fluorogen and an anticancer drug could be prepared and stabilized efficiently by the mixture of PF127/PF127-AA that give these nanoparticles superior targetability toward MDA-MB 231 and 4T1 cancer cells

concerning nontargeted nanoparticles. To the best of our knowledge, this is the first report of NLCs doped with FMN for antineoplastic activity. Furthermore, the extensive studies that were conducted will propound the aggregation-induced emission fluorogen-based NLC nanotheranostics for breast cancer therapy.

2. MATERIALS AND METHODS

2.1. Materials. *p*-Anisic acid, formononetin (FMN), glyceryl monooleate (GMO), Pluronic F127 (PF127), tetraphenylethylene (TPE), carbonyldiimidazole (CDI, 99%), (dimethylamino)pyridine ($\geq 99\%$), dicyclohexylcarbodiimide (DCC, $\geq 99\%$), *N*-hydroxysuccinimide (NHS, 99%), 3-[4,5-dimethylthiazol-2-yl]-2,5-diphenyltetrazolium bromide (MTT), propidium iodide (PI), and RNase were purchased from Sigma-Aldrich (St. Louis, MO), whereas Annexin V apoptosis kit was obtained from Merck. High-performance liquid chromatography (HPLC) solvents, such as methanol, were purchased from Merck (India). All other chemical reagents were of analytical grade and obtained from commercial sources. Triple-distilled water was prepared from Milli-Q system (Millipore, Bedford).

2.2. Methods. **2.2.1. Synthesis and Characterization of Pluronic F127–Anisamide Conjugate (PF127-AA).** The conjugate between AA and PF127 was prepared by carbodiimide chemistry in the presence of DCC and NHS. In brief, amine-terminated PF127 (PF127-NH₂) and NHS-activated anisic acid (anisic acid-NHS) were separately prepared (see the [Supporting information](#) for the detailed synthesis procedure) and then anisic acid-NHS (44 mg, 0.176 mmol) was added gradually to PF127-NH₂ (500 mg, 0.0395 mmol) and triethylamine (3.95 mg, 0.0395 mmol) was dissolved in dichloromethane at 0 °C under constant stirring for 1 h. The reaction was allowed to proceed for 24 h at room temperature (RT). The resulting PF127-AA was recovered by precipitating in diethyl ether and dried in vacuum for 48 h. The product PF127-AA was characterized by proton NMR and Fourier transform infrared (FTIR) spectroscopy techniques (PerkinElmer Spectrum II). NMR spectra were recorded using Bruker DRX-300 (Bruker, Fallanden, Switzerland) at 300 MHz by dissolving in CDCl₃ and analyzed using TopSpin software package.

2.2.2. NLC NPs Preparation. GMO-based targeted liquid crystalline particles (AA-NLC-TF) were prepared by dispersing an appropriate amount of GMO in phosphate-buffered saline (PBS, pH 7.4) solution of PF127/PF127-AA mixture at 70 °C using an ultrasonic processor (Vibra-Cell VCX 750, Sonics & Materials, Inc.) attached with a microtip at 20% amplitude power for 10 min in pulse mode (5 s sonic pulses interrupted by 5 s breaks). Doped NLC NPs were obtained by dispersing the FMN (12.5×10^{-2} wt %) and TPE (1.3×10^{-2} wt %) in the melted GMO (60 mg/mL) before mixing with the Pluronic solution. The GMO and PF127/PF127-AA were mixed in a ratio of 92:8 by weight. The final concentration of PF127/PF127-AA in solution was around 0.46 wt %. Similarly, nontargeted nanoparticles (NLC-TF) were prepared using PF127 as a stabilizer. The resulting white milky dispersion was stored at RT for future experimentation.

2.2.3. Determination of Loading (LE) and Entrapment Efficiency (EE) of NLC NPs. The LE and EE of FMN and TPE in NLC-TF and AA-NLC-TF were determined by calculating the free and total amount of FMN and TPE in the formulation. Briefly, 2 mL of NLC dispersion was loaded into a dialysis membrane (molecular weight cut-off (MWCO) 12 kDa) and dialyzed against Milli-Q water (1000 mL) for 4 h at RT by replacing the water every 1 h. After 4 h, NLC dispersion purified from the nonencapsulated drug was obtained. A similar method was followed for the determination of TPE content. By disrupting the NLC NPs with acetonitrile/methanol mixture, FMN and TPE contents were quantified, respectively, at 259 and 361 nm using the validated RP-HPLC method (Shimadzu, Japan) (see the [Supporting information](#) for HPLC method).³²

%LE was determined by eq 1

$$\%LE = \frac{W_{TP} - W_{UP}}{W_{TL}} \times 100 \quad (1)$$

where W_{TP} , W_{UP} , and W_{TL} are weights of total payload, unbound payload, and total lipid, respectively.

% EE was determined by eq 2

$$\%EE = \frac{W_{NLC}}{W_T} \times 100 \quad (2)$$

where W_{NLC} is the weight of FMN/TPE entrapped in NLC and W_T is the total weight of FMN/TPE added to the NLC formulation.

2.2.4. Quasi-Elastic Light Scattering (QELS) Experiments. At 25 ± 0.1 °C, the particle size and ζ potential of the nanoparticles were determined using Nano ZS 2000 (Malvern Instruments, Malvern, U.K.). The NLC formulations were diluted 1:100 times before the measurements of optimal sensitivity. All of the measurements were done in triplicate. The software available in Malvern Instruments (CONTIN algorithm) was used, and particle size values were reported as Z-average particle diameter. The width of hydrodynamic diameter distribution is indicated by polydispersity index (PDI).

2.2.5. Small-Angle X-ray Scattering (SAXS) Studies for Phase Identification. The phase identity and internal structure parameters of the NLC NPs were measured on a S3-Micro SAXS/SWAXS camera system (HECUS X-ray Systems, Graz, Austria) equipped with a one-dimensional position-sensitive detector (HECUS PSD50M) containing 1024 channels of width $54.0 \mu\text{m}$. Cu K α radiation (wavelength, 1.54 \AA) was provided by a GeniX X-ray generator. Measurements were performed in quartz flow cell; the temperature was controlled by a Peltier system. Samples were maintained at 25 °C for 30 min before experimenting. The working q range used to detect signals was 0 – 0.6 \AA^{-1} , where the length of scattering vector q is defined by eq 3.³³ The symmetry of the liquid crystalline nanoparticles was determined by the relative q positions of the Bragg peaks shown in the scattering curves. The water channel radius, r_w , of the inverse hexagonal (HII) phase of NLC NPs was calculated using eq 4.^{13,34}

$$q = \left(\frac{4\pi}{\lambda} \right) \left(\frac{\sin \theta}{2} \right) \quad (3)$$

where θ is the scattering angle relative to the incident X-ray and λ is the wavelength at which X-rays are generated.

$$r_w = a(1 - \phi_{lip})^{1/2} \left(\frac{\sqrt{3}}{2\pi} \right)^{1/2} \quad (4)$$

where a is mean lattice parameter and ϕ_{lip} is the volume fraction of the dispersion phase.

2.2.6. Morphological Evaluation of NLC NPs. The morphology of NLC NPs was observed by various microscopic techniques.

2.2.6.1. Transmission Electron Microscopy (TEM). Briefly, the samples were placed over a carbon-coated copper grid and let to settle for 5 min. Then, the dried samples were negatively stained with 2% aqueous solution of uranyl acetate. Finally, the samples were observed on Jeol TEM 1400 (JEOL Ltd., Tokyo Japan).³⁵

2.2.6.2. Atomic Force Microscopy (AFM). APE Research AFM (AFM, APCER, Italy) was used for the morphological evaluation of NLC NPs in a noncontact mode using cantilever ($\mu\text{mash NSC15/AIBS}$) of $125 \mu\text{m}$ length, $35 \mu\text{m}$ width, and $<10 \text{ nm}$ tip radius. Briefly, a drop of $10 \mu\text{L}$ of NLC samples was placed on a coverslip and allowed to air dry. After carefully removing the excess aqueous phase only and not allowing the sample to get completely dry, the samples were viewed under an atomic force microscope with a force constant of 45 N/m .^{36–38}

2.2.6.3. Cryogenic Force Emission Scanning Electron Microscopy (Cryo-FESEM). For the morphological analysis using ZEISS ULTRA plus Cryo-FESEM (Carl Zeiss International, Germany), selected NLC formulations were transferred using a micropipette into brass rivets and plunge-frozen in liquid nitrogen at -190 °C (Alto 2500, Gatan) immediately. Subsequently, the samples were transferred under vacuum to the cryo-chamber of the microscope, where the temperature was maintained at -150 °C, followed by fracturing frozen samples using a knife maintained at -150 °C to reveal a clear surface. Then, the samples were sublimed for 15 min at -90 °C to

etch any water on its surface following fracture. Conductive platinum was used to sputter-coat at 11 mA for 50 s to deposit a thin layer on top of the sample. The sample was then transferred under vacuum into the Cryo-FESEM microscope chamber and imaged at an accelerating voltage of 3 kV and a working distance of 5–6 mm.

2.2.7. Photophysical Characterization. The photophysical characterization of NLC nanoparticle dispersions was conducted by prior dilution with Milli-Q water (1:100). UV–vis absorption spectra were recorded using a UV-1700 PharmaSpec UV–vis spectrophotometer (Shimadzu Corporation, Tokyo, Japan). Fluorescence measurements were recorded on Agilent Cary Eclipse Fluorescence Spectrophotometer (Agilent Technologies, CA). The fluorescence quantum yields on TPE were measured using rhodamine 6G dissolved in ethanol as a standard ($\Phi_{\text{ref}} = 0.94$).

2.2.8. In Vitro Drug Release Studies. The release of FMN and TPE from AA-NLC-TF was assessed using a dialysis bag method at 37 °C. In short, NLC NPs containing equivalent amount of FMN (2 mg) and TPE (0.2 mg) were loaded into a dialysis bag (Spectra/por, MWCO 12 kDa, CA) and then the bag was immersed in 100 mL of phosphate-buffered saline (PBS, pH 7.4 or pH 5.5) containing 0.1% v/v Tween 80 at 37 ± 0.5 °C to maintain sink condition and continuously rotated at 100 rpm. The samples were collected from the sink and replaced with fresh PBS at regular intervals. Finally, the concentrations of FMN and TPE were analyzed using the HPLC method. The release rate of the payload was calculated using eq 5

$$RR = \left(\frac{wd}{wD} \right) \times 100 \quad (5)$$

where wd is the amount of payload released after specific time point and wD is the total amount of payload used in the release study.³⁹

2.2.9. Stability Studies. The physical stability of the optimized formulations was measured at 25 °C for change in the particle size and PDI at regular time intervals. Further, to determine the in vivo fate of AA-NLC-TF, the stability was measured in biologically relevant media by incubating the nanoparticles in 10% fetal bovine serum (FBS) and the changes in size with time were monitored using QELS.

2.2.10. Hemolysis Assay. Hemolytic toxicity study was performed according to a reported protocol with slight modifications.⁴⁰ Fresh blood was collected in heparinized vials centrifuged at 3000 rpm for 10 min to separate the red blood cells (RBCs). Sediment RBCs were washed with PBS (pH 7.4) and then diluted with PBS to obtain 2% hemocrit. Blank nanoparticles, free drug, NLC-TF, and AA-NLC-TF were incubated with equal volume of RBC suspension at a various concentrations of FMN for 2 h at 37 °C. After incubation, the samples were centrifuged for 10 min at 3000 rpm and the supernatants were drawn to quantify the hemoglobin content using a microplate reader (PowerWave XS, Biotek, VT) at 540 nm. RBC treated with 1% Triton-X served as positive, whereas PBS (pH 7.4) treated RBC served as negative control.

2.2.11. Cell Culture. MDA-MB 231, human breast cancer cell line, was obtained from American Type Culture Collection (Rockville, MD), whereas 4T1 cells were obtained from National Center for Cell Science (NCCS, Pune, India). Cells were cultured in Roswell Park Memorial Institute medium-1640 (RPMI-1640) with 10% (v/v) FBS, along with $100 \mu\text{g/mL}$ streptomycin and 100 U/mL penicillin. All of the cancerous cells were cultured in an incubator (Thermo Scientific) at 37 °C under 90% relative humidified environment of 5% CO_2 .

2.2.12. Cellular Cytotoxicity Studies. In vitro cytotoxicity of free FMN, NLC formulation (blank NLC loaded with an imaging agent, NLC-TF, AA-NLC-TF) was assessed using 3-(4,5-dimethylthiazol-2-yl)-2,5-diphenyltetrazolium bromide (MTT) assay on MDA-MB 231 and 4T1 cells separately. In brief, MDA-MB 231 and 4T1 cells were seeded in 96-well plates separately (3×10^3 cells/well) in $100 \mu\text{L}$ of RPMI containing 10% FBS and kept for incubation at 37 °C in 5% CO_2 . Experiments were carried out when cells had reached 90% confluence. The free drug and the different formulation of NLC were added to the cells in RPMI with 2% FBS at different concentrations (ranging from 1 to $60 \mu\text{M}$ equivalent concentration of FMN/TPE) and incubated for 48 h at 37 °C. After 48 h, media was removed and

cells were treated with 20 μL of MTT (5 mg/mL) reagent for 4 h. Then, 100 μL of dimethyl sulfoxide (DMSO) was added to dissolve the formed formazan crystals. The color developed was measured on an automated microplate reader at 570 nm, and its absorbance is proportional to the number of viable cells. Untreated cells served as a control in comparison to the treated cells, and the results are shown as the percentage of cell viability. All experiments were carried out thrice ($n = 3$). Data were expressed as a mean \pm standard deviation (SD).

Cytotoxicities of blank and AA-NLC-TF NLC NPs were also determined on J774.2 cells to evaluate the biosafety of the developed liquid crystalline particles.

2.2.13. Cellular Uptake and Cell Imaging Studies. **2.2.13.1. Confocal Laser Scanning Microscopy (CLSM).** The application of anisamide-conjugated NLC NPs was investigated for the targeted intracellular imaging as well as cellular uptake by confocal microscopy. MDA-MB 231 cells and 4T1 cells were seeded on polylysine-coated coverslips placed in 12-well plates at a density of 2×10^4 cells per well in 1 mL of RPMI with 10% FBS and incubated for 24 h. The cells were then treated with media containing AA-NLC-TF and NLC-TF particles at equivalent concentrations of TPE (0.25 μM), FMN (3 μM), and rhodamine B (20 μM) incubated for 4 and 12 h. After incubation, excess nanoparticles were removed by washing with PBS and then cells were fixed with 4% formaldehyde solution for 15 min at RT. Finally, the coverslips were mounted on the glass slides sealed with mounting media and observed under a confocal microscope (Carl Zeiss LSM510 META, Carl Zeiss, Germany). Plan-Apochromat 63 \times /1.40 oil DIC objective lens with an excitation of 405 nm for TPE (argon 405/488 laser lines) and 561 nm for rhodamine B (diode-pumped solid-state laser lines), bandpass filter 420–480, and long pass filter 575 were used.

2.2.13.2. Flow Cytometry. For the assessment of quantitative uptake of nanoparticles by MDA-MB 231 and 4T1 cells, flow cytometer (BD Biosciences, FACSARIA, Germany) was utilized. The cells were seeded at a density of 5×10^5 cells per well in a six-well plate and incubated for 24 h, followed by treatment with the formulation described above. Following incubation for the respective time intervals, the cells were washed with PBS, harvested, and then suspended in 0.5 mL of PBS. Cell-associated fluorescence was used for the quantitative determination of nanoparticles uptake using 405 nm laser with a 450/20 bandpass filter to collect the data. The receptor specificity of the AA-NLC-TF nanoparticles was further evaluated through receptor blocking studies using flow cytometry. MDA-MB 231 cells were preincubated in 100 μM AA in complete media for 2 h before the addition of the above-mentioned NLC NPs.

2.2.14. Cell Cycle Analysis. For the cell arrest, propidium iodide (PI)-based assay was used to evaluate the effect of FMN on MDA-MB 231 cells by employing a flow cytometer (BD Biosciences, FACS Calibur, Germany). MDA-MB 231 cells were grown in six-well plates (1×10^6 cells/well) and incubated overnight at 37 $^\circ\text{C}$. Adherent cells were treated with free FMN, NLC formulations containing an equivalent concentration of FMN (3 μM) along with fresh media and incubated for 24 h. After a predefined time interval, the cells were washed, harvested, and fixed with the precooled ethanol (70%) at 4 $^\circ\text{C}$ for 2 h. After fixing, the cells were centrifuged and resuspended in 500 μL of PBS (pH 7.4) and treated with ribonuclease A (100 $\mu\text{g}/\text{mL}$) and PI (50 $\mu\text{g}/\text{mL}$) for 30 min in the dark. Cell-based fluorescence was measured using a flow cytometer to appraise the phases of cell cycle arrest.

2.2.15. Apoptosis. MDA-MB 231 cells were incubated at a density of 1×10^5 per well in a six-well plate for 24 h and treated with media containing different treatments of FMN equivalent to (3 μM). After 48 h incubation, the cells were harvested, washed with PBS twice, collected, and resuspended in 500 μL of 1 \times binding buffer and stained with Annexin V–fluorescein isothiocyanate (FITC) (5 μL) and propidium iodide (10 μL) for 20 min under dark conditions and analyzed for early and late apoptosis using a flow cytometer (BD Biosciences, FACS Calibur, Germany). Untreated cells were used as control over treated cells. The experiments were done in triplicate.

2.2.16. Mitochondrial Membrane Potential (MMP). To measure MMP of MDA-MB 231 cells, JC-1 dye (5,5',6,6'-tetrachloro-1,1',3,3'-

tetraethylbenzimidazolylcarbocyanine iodide) (Molecular Probes, Eugene, OR) was used. Initially, the cells were grown in 12-well plates at a density of 1×10^5 cells/well, followed by treatment with free FMN, blank NLC, and targeted and nontargeted nanoparticles at an equivalent drug concentration of FMN (3 μM) for predetermined time intervals. Subsequently, media was removed and cells were washed with PBS and treated with JC-1 solution (15 $\mu\text{g}/\text{mL}$). Cell-associated fluorescence was measured by the flow cytometer. PBS-treated cells served as negative control, whereas 50 nM carbonyl cyanide 4-(trifluoromethoxy) phenylhydrazone (FCCP)-treated cells were used as positive control.

2.2.17. Reactive Oxygen Species (ROS) Generation. Dichlorodihydro-fluorescein diacetate (DCFH-DA) assay was performed to determine the ROS levels in the treated cells. Briefly, MDA-MB 231 cells (2×10^5 cells/well) were grown in six-well plates and then treated with 3 μM equivalent FMN containing NLC formulation, free drug, and blank NLC. After 12 and 24 h of treatment, the cells were exposed to 10 μM DCFH-DA and incubated for 0.5 h at 37 $^\circ\text{C}$. After incubation, the cells were washed twice with PBS, trypsinized, and resuspended in PBS. Finally, the ROS production level was determined by the fluorescence intensity of dichlorofluorescein (DCF) using the flow cytometer (BD Biosciences, FACS Calibur, Germany). Untreated cells were used as control, and all of the experiments were repeated thrice ($n = 3$).

2.2.18. In Vivo Studies. All of the animals were obtained from the National Laboratory Animal Center (NLAC) facility, CSIR-Central Drug Research Institute (CDRI), Lucknow. All of the animal experiments were done with prior approval (IAEC approval No. IAEC/2017/159) by the Institutional Animal Ethical Committee (IAEC) of CSIR-CDRI, India.

2.2.19. Tumor Model. Female BALB/c mice (4 weeks old; weight, 18–20 g) were selected and acclimatized for a week in 12 h light and dark condition under controlled temperature (24 $^\circ\text{C}$). The mice were injected subcutaneously with about 100 μL of cell suspension containing 5×10^6 4T1 cells at the mammary gland near to the lower right quadrant of the abdomen. After inoculation, regular observation of animals was made, and when the tumor grew to about 100 mm³, studies were started.⁴¹

2.2.20. In Vivo Optical Imaging. An in vivo imaging system was used to study the accumulation of AA-NLC-TF in the tumor-bearing mice inoculated with 4T1 cells. NLC-TF and AA-NLC-TF containing (10 mg FMN equiv/kg) and PBS were intravenously (iv) administered when tumors reached about 100 mm³ in volume. The mice were anesthetized with 2% isoflurane/air mixture, and in vivo optical images were taken within the predetermined time with an excitation filter of 430 nm and an emission filter of 620 nm. The exposure time was 5 s per image. The final concentration of TPE used was 1 mg/kg. Signal intensity of the images was quantified as the radiant efficiency within a region of interest prescribed over the tumor site. After imaging, the mice were sacrificed and the major organs of tumor, brain, heart, lungs, liver, spleen, and kidney were harvested and imaged under the same conditions to know the distribution of nanoparticles. Fluorescence images of the mice were acquired with the IVIS Kinetic Imaging System (Caliper Life Sciences), and the images were analyzed with Living Image software version 4.4 (Caliper Life Sciences).

2.2.21. In Vivo Antitumor Efficacy. For in vivo antitumor efficacy studies, the mice were divided into four groups with six animals in each group under regular observation once. When tumor volume reached 100 mm³, the mice were injected with iv route free FMN, NLC-TF, AA-NLC-TF (at an equivalent dose of 10 mg/kg FMN), and PBS as control every 2 days for seven times. Tumor volumes were measured for individual animals in all experiments every 2 days with a digital caliper in two dimensions and calculated using the following formula: volume = (length \times width²)/2. The mice were sacrificed on the 20th day, and the tumors were weighed to calculate the tumor growth inhibition rate (TIR) by the following formula: TIR = $\{(1 - (\text{mean volume of treated tumors})/(\text{mean volume of control tumors})) \times 100\}$.

2.2.22. Survival Analysis. For the survival analysis, the animals were divided into four groups similar to the tumor regression study, and six

Scheme 1. Schematic Illustration of Synthetic Steps for PF127-AA and Schematic Illustration of AIE-Based Active Bioimaging in Vitro and in Vivo

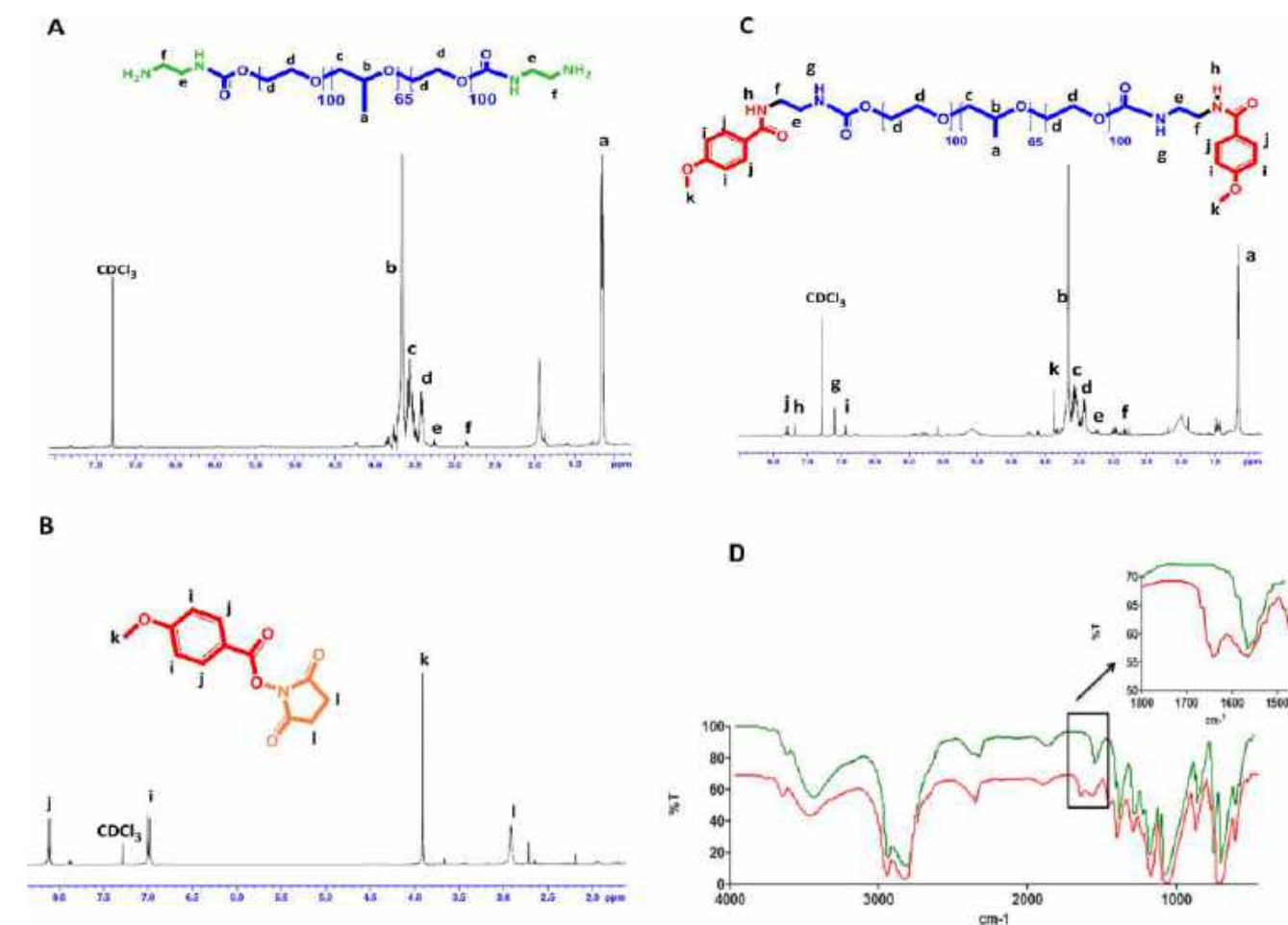
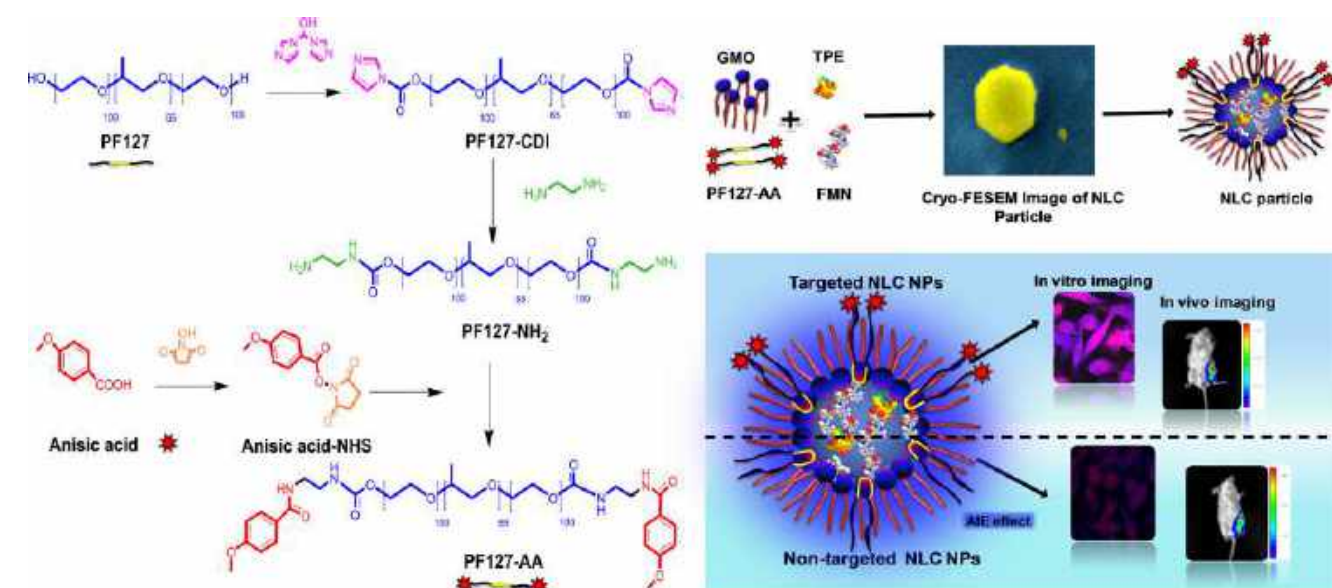


Figure 1. Characterization of conjugate by ¹H NMR (A) PF127-NH₂; (B) anisic acid-NHS; (C) PF127-AA; and (D) FTIR spectra of PF127-AA.

animals were taken in each group for a separate experiment. The animals were observed daily when the tumor volume reaches 100 mm³; treatment started as per the protocol mentioned above, and survival analysis study was conducted for up to 30 days. The survival rate of animals in these four different groups was measured during this

period and analyzed using GraphPad Prism 5.0 software. Survival curves were evaluated using the log-rank (Mantel–Cox) test method.

2.2.23. Statistics. Statistical significance of the data was analyzed by one-way analysis of variance, and probability values <0.001 or <0.05 were considered significant. All of the calculations were done using the

Table 1. Characteristics of NLC NPs^a

NLC NPs	particle size (nm)	PDI	ζ potential (mV)	% LE		% EE	
				TPE	FMN	TPE	FMN
blank	112.0 \pm 5.36	0.258 \pm 0.03	-25 \pm 2.09				
NLC-TF	115.7 \pm 4.36	0.101 \pm 0.012	-22 \pm 1.28	0.22 \pm 0.03	2.12 \pm 0.06	96 \pm 2.15	96 \pm 3.20
AA-NLC-TF	127.0 \pm 6.95	0.242 \pm 0.015	-24 \pm 2.56	0.21 \pm 0.01	2.15 \pm 0.03	95.27 \pm 1.15	97 \pm 2.89

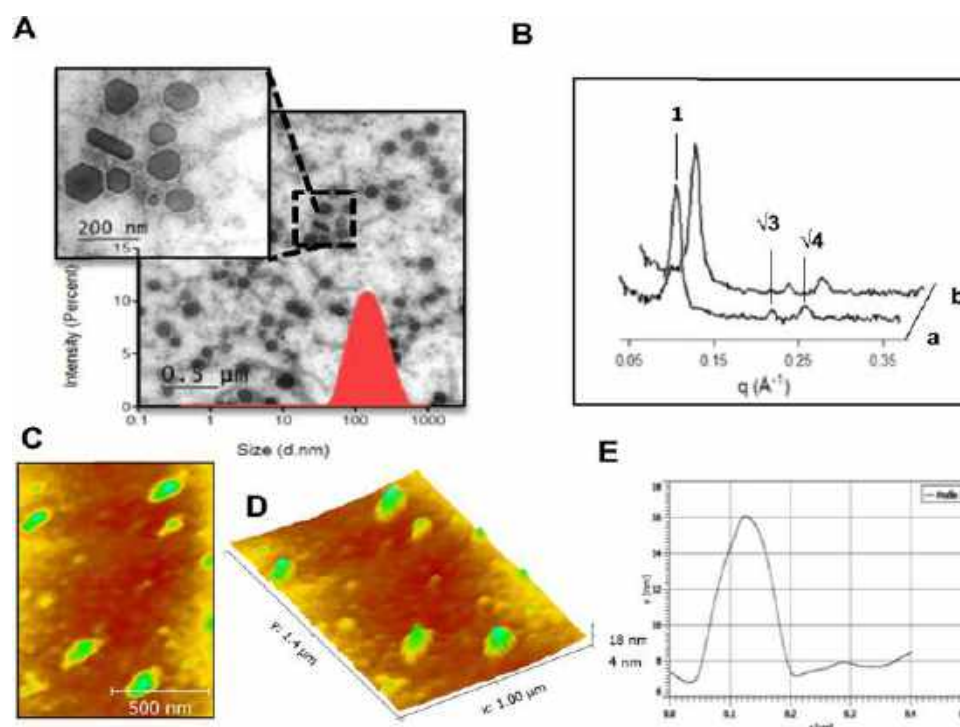
^aAll values are represented as mean \pm SD.

Figure 2. Size and morphological characterization of NLC NPs by (A) TEM (scale bar, 200 nm) and particle size distribution of AA-NLC-TF particles. (B) SAXS intensity plots of (a) blank NLC particles and (b) AA-NLC-TF. AFM images of AA-NLC-TF particles (C) two-dimensional image (scale bar, 500 nm) and (D) 3D view. (E) Height profile.

GraphPad Prism version 5.0 for Windows (GraphPad Software, San Diego, CA).

3. RESULTS

3.1. Preparation of AIE Fluorogen-Based Targeted and Nontargeted NLC Nanotheranostics. Here, we attempted to formulate the nanotheranostics to track down the tumor location and for chemotherapy. For this purpose, GMO-based NLC NPs stabilized by PF127/PF127-AA mixture was loaded with the FMN and TPE. The synthetic scheme and proposed model illustrating the AIE-based active bioimaging in vitro and in vivo are shown in Scheme 1. In brief, PF127-NH₂ was synthesized in the presence of CDI and ethylenediamine, and the conjugation of the amino group to the PF127 terminal was confirmed by the trinitrobenzene sulfonic acid assay (conjugation efficiency, 97%). Then, anisic acid-NHS was reacted with the amino end of PF127 to form PF127-AA. The successful conjugation of anisic acid to PF127-NH₂ was confirmed by ¹H NMR spectra, where the singlet peak at 7.10 ppm was the characteristic peak due to the amidic NH from the precursor PF127-NH₂ conjugate, whereas the peak at 7.68 ppm was due to the just formed amidic bond with anisic acid-NHS. Also, FTIR spectrum of PF127-AA, which displayed the carbonyl group of the amidic function at 1715.3 cm⁻¹, attested the presence of anisamide in the polymer chain. By

dissolving a known amount of PF127-AA in DMSO, UV absorbance at 260 nm was measured to determine the concentration of conjugated anisamide based on the calibration curve of anisamide plotted at 260 nm. The conjugation percentage of anisamide to PF127 was 94%. Subsequently, PF127 or PF127/PF127-AA mixture was used for the stabilization of GMO-based targeted and nontargeted NLC NP dispersions. ¹H NMR spectra of the reactants and synthesized PF127-AA are presented in Figure 1.

3.2. Physicochemical Characterization of NLC NPs.

First, the QELS method was used to determine the size and ζ potential of the nanoparticles. Results reported in Table 1 showed that a slight change in the hydrodynamic radii of nanoparticles was observed in QELS study. The mean particle size increased from 115.7 nm (100% PF127) to 127 nm (67% PF127 and 33% PF127-AA mixture) owing to increase in the amount of PF127-AA, and this growth suggested that the conjugation of anisamide to the PF127 modified the original steric stabilizing properties of the surfactant. Nonetheless, such a conjugation does not destabilize the nanoparticle delivery system. Thus, there were no major changes in the size and PDI of the NLC NPs during stability studies. The size of the nanoparticles obtained was also suitable for accumulation at the tumor site by enhanced permeability and retention effect, and they were found to be in good agreement with the dimensions

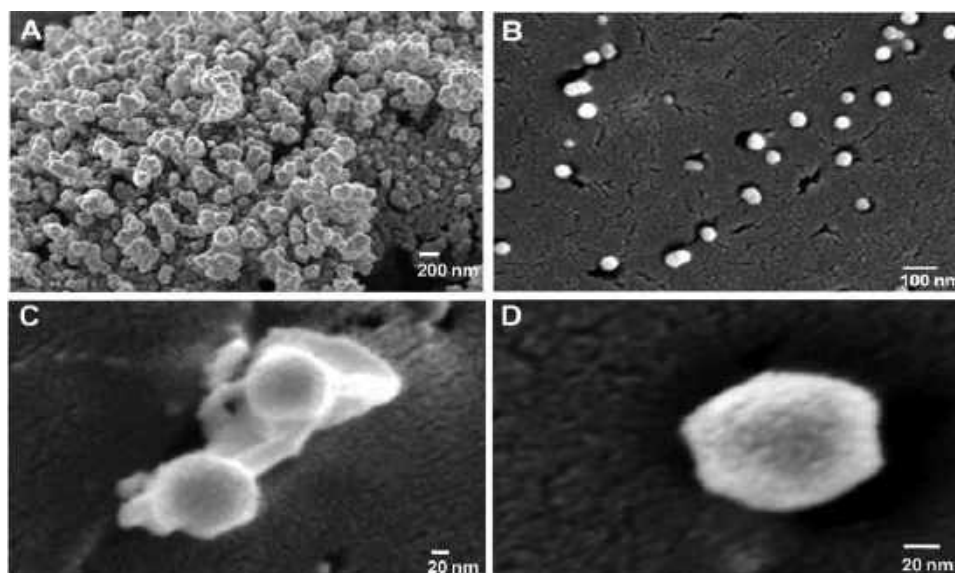


Figure 3. Cryo-FESEM photoimages of NLC NPs: blank nanoparticles (A) before dilution (scale bar, 200 nm) and (B) after dilution (scale bar, 100 nm); (C) blank nanoparticles (scale bar, 20 nm); and (D) AA-NLC-TF nanoparticles (scale bar, 20 nm).

obtained with Cryo-FESEM, TEM, and AFM images (Figures 2 and 3). After loading the drug and AIEgen, ascribed to their hydrophobic nature, they strongly intercalated within the lipid core of the NLC NPs. The entrapment efficiencies (EE) of the drug and AIEgen in AA-NLC-TF were found to be 95 and 97% (Table 1), respectively. Pertaining to measured ζ potential values, they were found to be in the range of -22 to -25 mV. Although GMO, PF127, and PF127-AA do not carry any inherent charge, on the other hand, the negative charge of the nanoparticles could be due to the adsorption of the hydroxide ions of the polarized water layer surrounding its outer surface.⁴²

Further, we have investigated the phase at which liquid crystalline particles exist through SAXS analysis. As can be seen from the SAXS data (Figure 2B), the Bragg peaks positioned at $1:\sqrt{3}:\sqrt{4}$ ratio represent an HII phase, the targeted nanoparticles (AA-NLC-TF) retained the hexagonal structure found in the blank NLC prepared with the 100% PF127 with no significant change in the lattice parameter even after substituted with 67% PF127 and 33% PF127-AA mixture as well as due to loaded cargo (FMN and TPE). Structural parameters like lattice parameters and water channel radii of NLC NPs are reported in Table 2.

Table 2. Structural Parameters of NLC NPs Determined at 25 °C^a

NLC NPs	lattice parameter, a (Å)	water channel radii, r_w (Å)
blank particles	59.4 ± 0.4	31.0 ± 0.3
AA-NLC-TF	61.0 ± 0.2	33.1 ± 0.2

^aAll values are represented as mean \pm SD.

3.3. Morphological Evaluation of NLC NPs. In this study, we have employed TEM, AFM, and Cryo-FESEM to observe the morphology of NLC NPs. Inspection of NLC particles through TEM revealed that the particles possessed hexagonal symmetry. Typically, HII phase liquid crystalline particles consist of water-filled continuous cylindrical lipid matrix arranged in the hexagon shape, and as shown in the TEM photoimage (Figure 2A), when viewed in two dimensions, the lateral view of these NLC NPs will be

observed as a rod-shaped particle. These nanoparticles have also been imaged by AFM, where the size and morphology of the particles showed broad agreement with the TEM images (Figure 2C–E). Concerning development in the field of electron microscopy, Cryo-FESEM is used to determine the interparticle structure as well as three-dimensional (3D) image of the dispersed liquid crystalline particles.^{43,44} Usually, information on interparticle confined nanostructure is obtained when using Cryo-TEM, which is a widely used method for characterization of a variety of self-assembled nanostructures as a complement to QELS, SAXS, or SANS. Conductiveness of Cryo-FESEM technique allows vitrified samples to be imaged as same as Cryo-TEM, but sublimation of surface water and sputter-coated platinum reveals the 3D structure of nanoparticles. The 3D view exposed by the Cryo-FESEM showed that the NLC NPs adopted a hexagon-like structure as observed in TEM images (Figure 3). The average sizes obtained from the different techniques are 98.30–135.5 nm (TEM), 110.0–133.2 nm (AFM), and 90–140 nm (Cryo-FESEM).

3.4. Photophysical Studies. After the fabrication of nanoparticles, it is necessary to confirm the yielded nanoparticles capable of preserving the AIE effect. As shown in Figure 4A, due to the AIE property of TPE trapped in the crystalline core, liquid crystalline particles show bright blue emission under 365 nm UV light. Indeed, high-fluorescence quantum yield (0.29) was obtained for the TPE loaded in the nanoparticles. The presence of AA-NLC-TF nanoparticles in water was also confirmed by shining a laser beam through the nanoparticle solution to observe the Tyndall effect (Figure 4C). The absorption and fluorescence emission spectra of AA-NLC-TF were measured and are shown in Figure 4D,E. The peak shown at 342 nm might be attributed to the characteristic peak of TPE aggregates in water, and at the same equivalent concentration in NLC, the blue shift of the TPE peak is due to restriction of the intramolecular rotation (RIR) of the phenyl groups as well as the increased hydrophobicity of the local environment due to nanoaggregates. The maximum absorption and emission peaks of the liquid crystalline particles are found at 372 and 476 nm, respectively. This large Stokes shift (>104 nm), which can minimize the interference from the self-

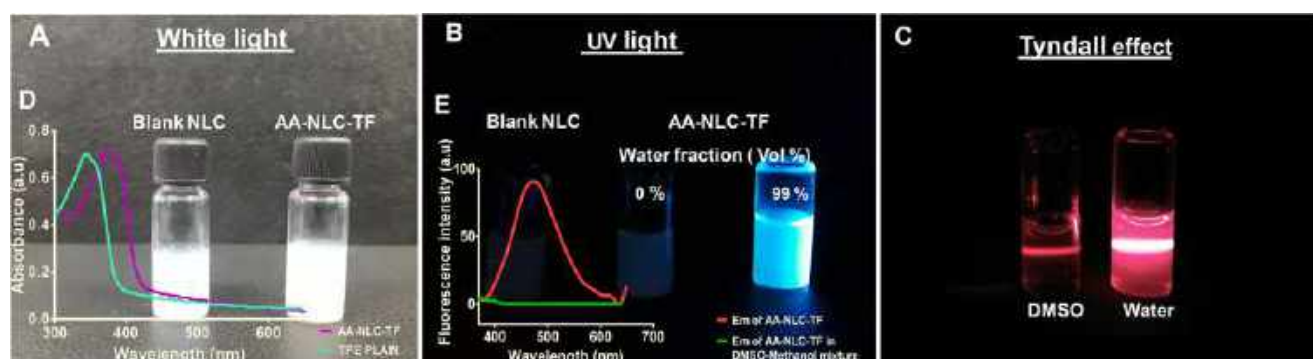


Figure 4. Fluorescence photographs of NLC dispersion (A) without UV illumination and (B) upon UV illumination (365 nm) and dispersion in DMSO and DMSO/water mixture (99 vol % of water), showing a typical AIE phenomenon. (C) Tyndall effect of AA-NLC-TF in DMSO and water. (D) Absorption spectrum of TPE plain and AA-NLC-TF. (E) Fluorescence spectrum of AA-NLC-TF in water and DMSO/methanol mixture excited at wavelength of 330 nm.

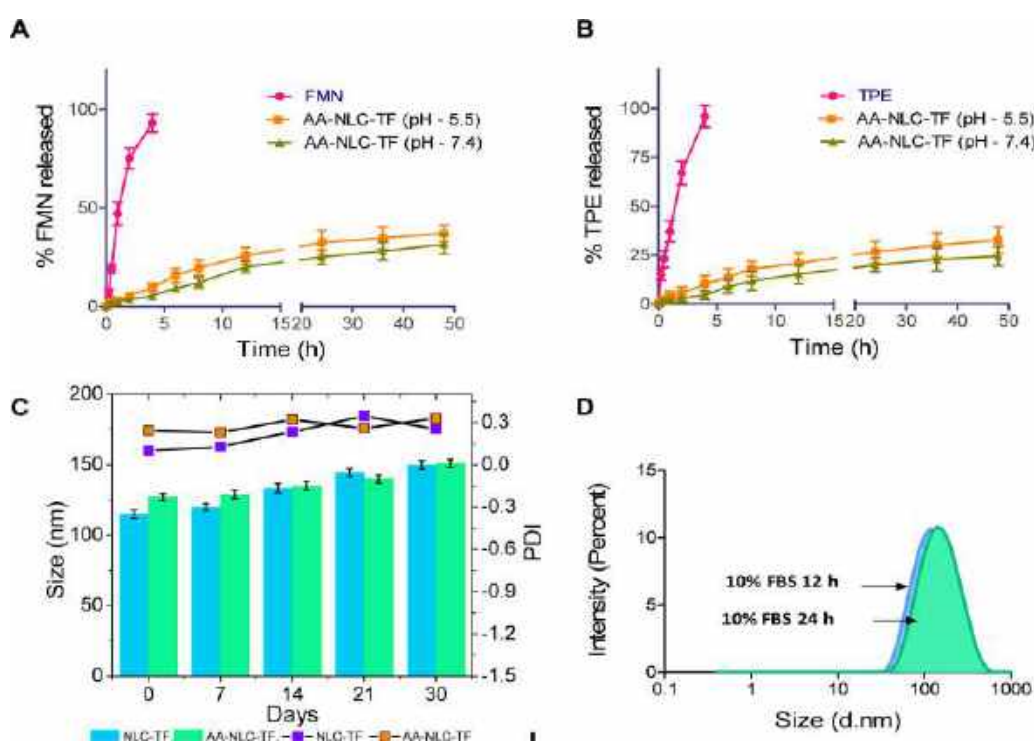


Figure 5. In vitro drug release profiles of (A) FMN from AA-NLC-TF and (B) TPE from AA-NLC-TF. Drug release study was conducted in PBS (pHs 7.4 and 5.5 at 37 °C) supplemented with 1% v/v Tween 80. (C) Data representing the physical stability of NLC-TF and AA-NLC-TF carried out in PBS (pH 7.4) at 25 °C for a period of 1 month. (D) serum stability of AA-NLC-TF for 12 and 24 h. Data are represented as mean \pm SD of three experiments.

absorption, indicates the suitability of AA-NLC-TF nanoparticles for the potential bioimaging application.

3.5. In Vitro Drug Release Studies. The release profiles of FMN and TPE from AA-NLC-TF were recorded at two different pHs (7.4 and 5.5) using dialysis bag method to simulate blood and tumor-associated microenvironment. Free FMN and TPE dissolved in DMSO were also utilized as control, and a complete release ($90.23 \pm 3.60\%$ for FMN and $95.78 \pm 2.70\%$ for TPE) within 4 h was found for both the payloads. But FMN and TPE encapsulated in AA-NLC-TF showed a controlled release without burst release at both the pHs, and it was observed that the release of payloads at pH 5.5 was faintly faster than that at pH 7.4. Approximately, $37.82 \pm 3.22\%$ of FMN was released at pH 5.5 in 48 h, whereas at pH 7.4, $30.90 \pm 3.60\%$ was found to be released. However, in case

of TPE, 32.60 ± 2.80 and $24.39 \pm 2.30\%$ were found to be released at pHs 5.5 and 7.4, respectively, within 48 h. Increase in release at pH 5.5 can be attributed to phase inversion of the liquid crystalline nanoparticles under acidic condition (Figure 5A,B). However, this phenomenon will be beneficial under actual disease conditions for the NLC NPs to show better anticancer effect.

3.6. Stability Studies. The physical stability of the nanoparticles due to steric stabilizer PF127 does not change, whereas the content of PF127-AA increased in the AA-NLC-TF formulation. This was evident by the monitored size and PDI of the nanoparticles on stability studies conducted at 25 °C for 1 month in PBS (pH 7.4). As shown in Figure 5C, there was no aggregation or change in the size and PDI of the NLC NPs, which indicates the long-term storage stability of the

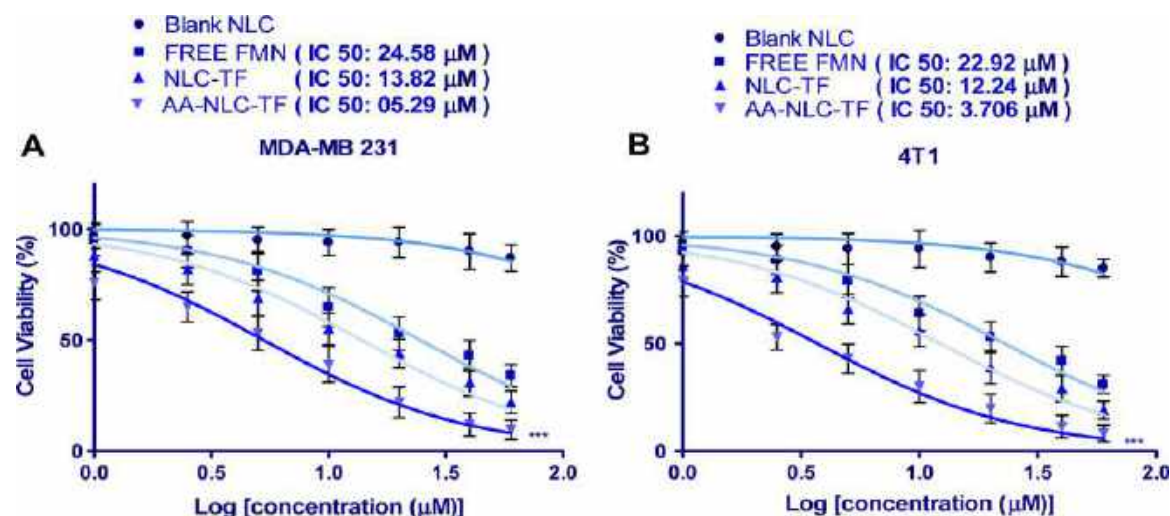


Figure 6. In vitro cell cytotoxicity analysis of (A) MDA-MB 231 and (B) 4T1 cells after treated 48 h with blank NLC NPs consisting of TPE equivalent to 1–60 μM, free FMN, NLC-TF, and AA-NLC-TF having FMN concentration equivalent to 1–60 μM. *** $P < 0.001$ vs the same dose of NLC-TF.

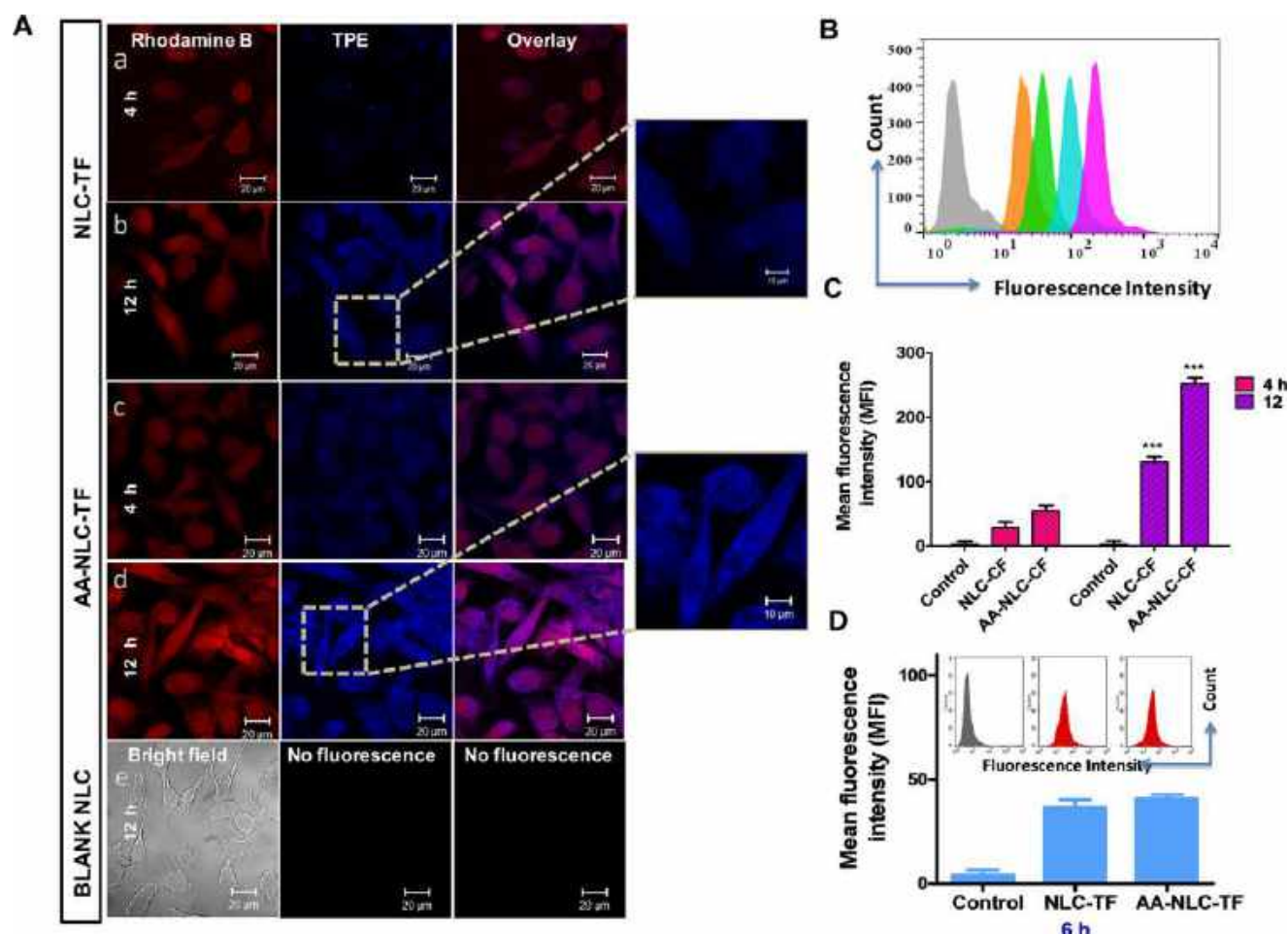


Figure 7. (A) CLSM images of live MDA-MB 231 cells treated with (a, b) AA-NLC-TF and (c, d) NLC-TF for 4 and 12 h; (e) blank NLC (scale bar, 20 μm). (B) Fluorescence intensity histograms of MDA-MB 231 incubated with AA-NLC-TF and NLC-TF (gray: control; 4 h group (orange: NLC-TF, green: AA-NLC-TF); and 12 h group (blue: NLC-TF, pink: AA-NLC-TF)). (C) Mean fluorescence intensity values of MDA-MB 231 cells after 4 and 12 h incubation of AA-NLC-TF and NLC-TF with equivalent concentrations of TPE (0.25 μM) and FMN (3 μM). (D) Receptor blocking studies carried out using flow cytometer showing the fluorescence intensity histogram and mean fluorescence intensity values of MDA-MB 231 cells after 6 h incubation of AA-NLC-TF and NLC-TF nanoparticles.

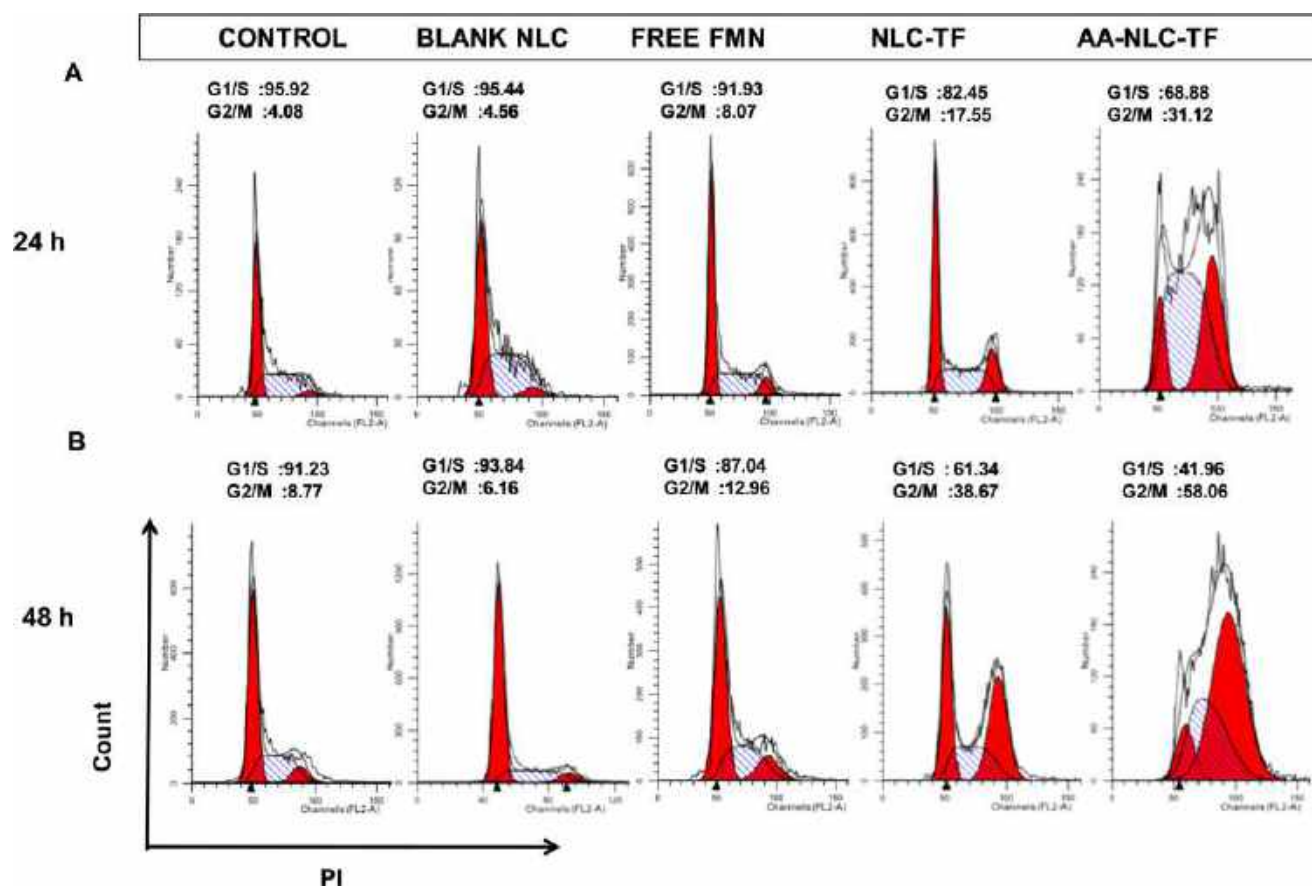


Figure 8. Representative cell cycle distribution in MDA-MB 231 cells (A) 24 h and (B) 48 h after incubation with blank NLC, free FMN, NLC-TF, and AA-NLC-TF at equivalent concentration of FMN (3 μ M).

formulation. Moreover, the biological stability of AA-NLC-TF was also analyzed in serum. The size of AA-NLC-TF nanoparticles was monitored in the presence of 10% FBS. If nanoparticles aggregate in serum, then they might aggregate upon injection also. As shown in Figure 5D, size of the particles remained stable upon 12 and 24 h incubation in serum, which indicates that the physical stability of NLC NPs does not alter upon interaction with serum proteins.

3.7. In Vitro Hemolytic Potential. Hemocompatibility assay of formulations was performed to know the in vitro toxicity, which also serves as a simple measure for predicting the blood compatibility for in vivo experimentation. Formulations containing equivalent concentration range of 5–30 μ M of FMN was used to assess the hemolytic potential of NLC formulation. FMN-loaded AA-NLC-TF showed ($4.1 \pm 1.3\%$) hemolysis at the highest equivalent concentration of FMN (30 μ M), and all of the drug-loaded nanoparticles showed lower hemolysis at different equivalent concentrations of FMN in comparison to positive control. These results manifested the hemocompatibility of AA-NLC-TF toward in vivo experimentation (Figure S1).

3.8. Cellular Cytotoxicity. To assess the anticancer activity of the free FMN and FMN containing formulation, MDA-MB 231 and 4T1 cell lines were chosen. As shown in Figure 6, FMN, NLC-TF, and AA-NLC-TF showed dose-dependent loss of cell viability in MDA-MB-231 and 4T1 cell lines. The cytotoxicity of cells treated with NLC-TF was greater than that of free FMN in both the cell lines but lesser than that of AA-NLC-TF treatment. The half-maximal inhibitory concentration

(IC_{50}) values of AA-NLC-TF nanoparticles were 4.64 and 2.61 folds less than those of the free FMN and NLC-TF after 48 h treatment in MDA-MB 231. Similarly, AA-NLC-TF showed 6.18 and 3.30 folds lesser IC_{50} than free FMN and NLC-TF in 4T1 cells, respectively. These results suggest that the anisamide conjugation with NLC particles amplified the therapeutic effect of the FMN by targeted drugs in the MDA-MB 231 and 4T1 cells. Additionally, biosafety of blank NLC and AA-NLC-TF was evaluated on J774.2 cells, and the results proved that this formulation is safe for normal cells and also demonstrated the targeted toxicity toward cancer cells (Figure S2). MTT assay was used to assess the cytotoxicity, and nonlinear regression analysis was used to calculate the IC_{50} values of the NLC NPs.

3.9. Cell Imaging and Intracellular Spatial Distribution of NLC NPs. Particulate uptake of nanocarrier by cancerous cells was confirmed by CLSM and flow cytometry. High sigma receptor expressing human breast cancer cell lines like MDA-MB 231 were selected for the uptake studies. The cells were treated with AA-NLC-TF and NLC-TF and observed under CLSM at various time points. As shown in Figure 7A, AA-NLC-TF showed significantly stronger blue fluorescence signals compared to the NLC-TF at all time points. The blue fluorescence was intensified in the cancerous cell after 4 h in the AA-NLC-TF group compared to the nontargeted NLC-TF-treated group, and the fluorescence was further intensified as time prolonged to 12 h. The difference in the intensities emphasized that the enhanced accumulation of AA-NLC-TF nanoparticles was mediated by the binding of AA conjugated nanocarriers to the sigma receptors (receptor-mediated

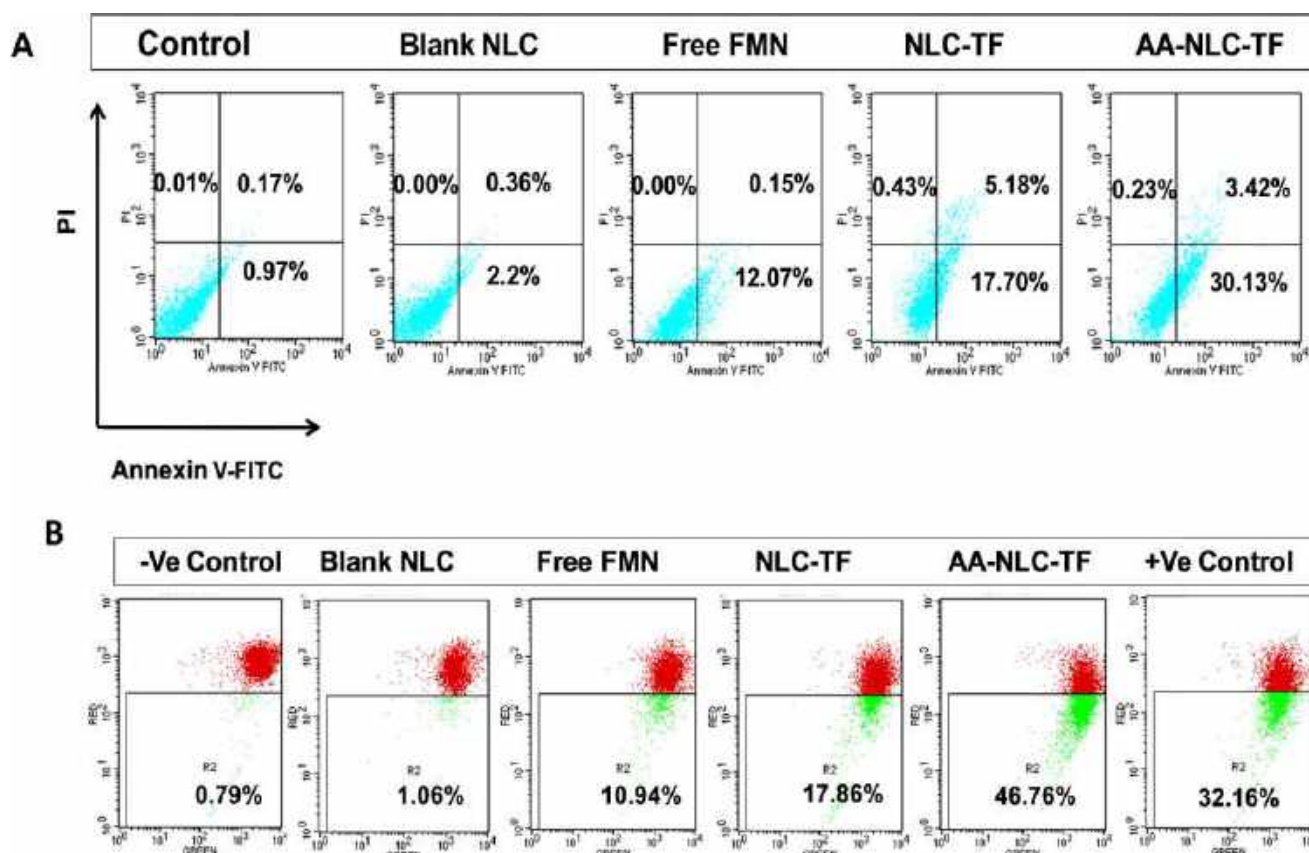


Figure 9. A) Dot plots representing the level of apoptosis in MDA-MB 231 cells after treatment with blank NLC, free FMN, NLC-TF, and AA-NLC-TF for 48 h. (B) Mitochondrial membrane potential of MDA-MB 231 cells generated after treatment with blank NLC, free FMN, NLC-TF, and AA-NLC-TF for 24 h. PBS-treated cells served as negative control, whereas FCCP-treated cells served as positive control.

uptake), whereas NLC-TF did not participate in receptor-mediated uptake, leading to lower fluorescence intensity in the MDA-MB 231 cell lines. For further confirmation of the intracellular trafficking of both the AA-NLC-TF and NLC-TF nanocarriers in the cancer cells, flow cytometric analysis (Figure 7B) was carried out as it analyzes the larger population of cells, and corroborative results were obtained with those of CLSM. As shown in Figure 7C, the higher mean fluorescence intensity of AA-NLC-TF showed that the uptake of AA-NLC-TF was higher than that of NLC-TF. To demonstrate the involvement of sigma receptors during endocytosis and to ensure this phenomenon, MDA-MB 231 cells were preincubated with 100 μ M free AA to saturate the receptors, followed by addition of both unmodified (NLC-TF) and surface-modified NLCs (AA-NLC-TF). After 6 h, we observed that the mean fluorescence intensity was similar in both types of formulations (Figure 7D). This analysis demonstrates the evidence of binding of AA to sigma receptors as well as the role of sigma receptors in enhancing the cellular uptake as well as the prospect of using this sigma receptor binding ligand for the diagnosis and targeted therapy for breast cancer.

Next, the uptake studies were also performed on 4T1 breast cancer cells (Figure S2). Similar to the results of MDA-MB 231 cells, the higher fluorescence intensity was observed under CLSM in AA-NLC-TF-treated group in comparison to NLC-TF. Results further confirmed by the flow cytometer also indicated the higher accumulation of AA-NLC-TF nanoparticles than the nontargeted nanoparticles.

3.10. Cell Cycle Arrest in MDA-MB 231 Cells. FMN induces the cell cycle arrest at G2/M phase in MDA-MB 231 cell lines via PI3K–Akt signaling pathway and triggers apoptosis in vitro and in vivo.⁴⁵ Figure 8 comprises the effect of free FMN and FMN-loaded NLC formulations along with blank NPs on MDA-MB 231 cell cycle for various time intervals. After 24 h, free FMN, NLC-TF, and AA-NLC-TF arrested the cells in G2/M phase compared to the control. Moreover, this percentage of cells in G2/M phase gradually increased in 48 h upon treatment with the above formulations. AA-NLC-TF (58.06%) showed much higher cell cycle arrest compared to free drug (12.96%) and NLC-TF (38.67%), which demonstrated the enhanced anticancer potential of targeted nanoparticles in cancer cells.

3.11. FMN-Loaded Targeted NLC NPs Enhance Apoptosis in MDA-MB 231 Cells. Despite apoptosis being the cause of various problems, it plays a vital role in the treatment of cancer as it is a popular target for various chemotherapy regimens. To investigate the effect of free FMN and FMN containing nanoparticles, quantitative evaluation of their apoptotic potential was done using flow cytometry with the aid of dual staining agents (PI and Annexin V–FITC). As shown in Figure 9A, the lower right quadrants of the dot plots represent the early apoptotic cells, whereas the upper right and upper left quadrants show the late apoptotic and necrotic cells, respectively. Results showed that the apoptotic effect of AA-NLC-TF was more pronounced than free FMN treatment. The apoptotic effect of AA-NLC-TF (33.55%) enhanced in comparison to NLC-TF (22.88%), free FMN (12.22%), and

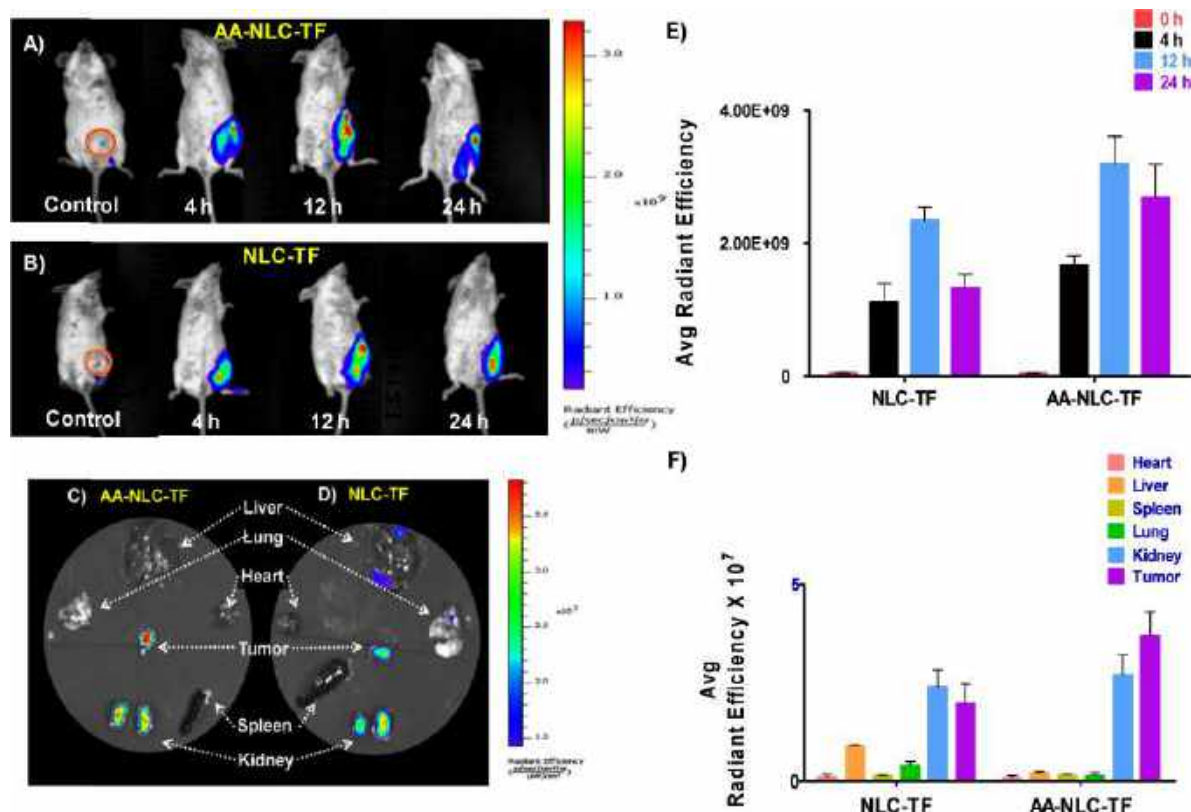


Figure 10. In vivo tumor imaging and tumor-targeting study after iv injection of NLC formulation. (A, B) Body imaging of targeted group and nontargeted group; tumor locations were marked by red circles. (C, D) Ex vivo imaging of major organs from 4T1 tumor-bearing mice at 12 h post injection of the above-mentioned group. (E) In vivo quantification of tumor-associated fluorescence signals of TPE-loaded NLC NPs. (F) Ex vivo quantification of fluorescence signals of TPE-loaded NLC NPs in other major organs. All data are shown as mean \pm SD ($n = 3$).

blank NLC (2.56%). As stated previously, sigma receptors played a vital role in the uptake of AA-NLC-TF. Reduced apoptotic effects observed after treatment with NLC-TF may be due to its nontargeting property, and the findings summarized in Figure 9A demonstrate the apoptotic effect of treatment regimens and free drug.

3.12. ROS Studies. The DCFH-DA assay quantitatively detects the intracellular production of ROS species like superoxide and hydrogen peroxide. Usually, mitochondrial ROS production occurs as natural products during metabolic processes, but their level increases in response to stress, which leads to damage to plasma membrane, DNA, and cellular damage. Eventually, it initiates the intrinsic apoptosis pathway of the cell. In this experiment, after treatment with both the types of NLC NPs and with free drug, the significant and increased production of ROS levels was detected. DCFH-DA, a permeant probe, was taken up by the attached cells and converted into fluorescent dichlorofluorescein (DCF) product, whose fluorescence intensity was measured using a flow cytometer. Results showed that AA-NLC-TF significantly increased the ROS level ($P < 0.001$) compared to NLC-TF and free FMN in 12 and 24 h, which indicated the negative impact of targeted nanoparticles on cellular viability. The mean fluorescence intensities of free FMN, NLC-TF, and AA-NLC-TF are shown in Figure S4.

3.13. In Vivo Optical Imaging. After superior in vitro activity, TPE- and FMN-loaded NLC NPs were examined for in vivo bioimaging applications. 4T1 metastatic breast cancer mice model, which was established by the subcutaneous injection of 4T1 cells into the BALB/c mice, was used as the

animal model. After intravenous injection of TPE-bearing nanoparticles (dose, 1 mg/kg TPE equivalent), the mice were imaged using IVIS Kinetic Imaging System (Caliper Life Sciences).

Figure 10A,B shows the time-dependent tumor accumulation of TPE-loaded nanoparticles in 4T1-cell-induced tumor-bearing mice. A high intense fluorescence was observed after 12 h post injection of AA-NLC-TF compared to the NLC-TF-treated group, indicating a higher localization of targeted nanoparticles (AA-NLC-TF) in the tumor tissue. The capability of the TPE-loaded AA-NLC-TF nanoparticles to illuminate the tumor tissue selectively with high contrast may be associated with dual factors. The first factor is the intense fluorescence of AIE fluorogen-TPE accumulated in the tumor, whereas the second factor includes active tumor-targeting ability of the nanoparticles by the AA ligand. In case of NLC-TF-treated animals, we observed relatively bright fluorescence at 12 h post injection, but it had diminished after 24 h. This relatively weak fluorescence of NLC-TF at tumor site was attributed to its nontargetability and consecutive low accumulation of NLC-TF NPs. Interestingly, the fluorescence signal of AA-NLC-TF persisted even after 24 h of injection, and its higher fluorescence intensity compared to NLC-TF, as shown in Figure 10E, clearly indicate that the TPE-encapsulated AA-NLC-TF nanoparticles can be used as an effective optical beacon for in vivo tumor diagnosis with high specificity and good fluorescence contrast.

The prominent active targeting of nanoparticles was also demonstrated using the ex vivo fluorescence imaging of excised tumor tissues and other major organs. As shown in Figure

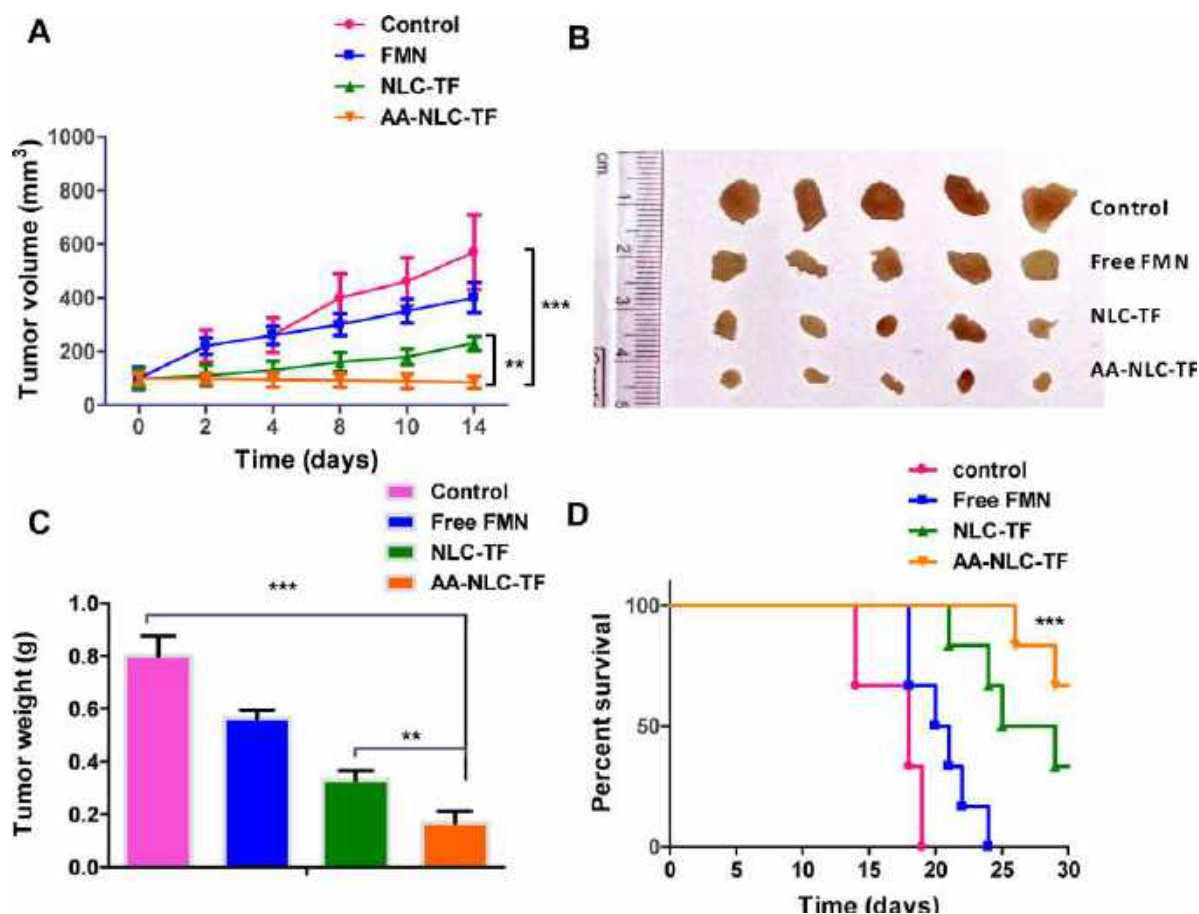


Figure 11. In vivo antitumor activity against 4T1 cells transplanted mammary tumor in BALB/c (FMN dose: 10 mg/kg body weight). (A) Tumor volume vs time at different time points of the study ($n = 6$). (B) Morphology of the tumors harvested at the end of the study. (C) Weights of the tumors excised at the end of the tumor regression study. (D) Survival rates of 4T1 tumor-bearing mice administrated with free FMN, NLC-TF, AA-NLC-TF, and PBS (control) ($n = 6$). (In tumor regression and survival studies, “day 0” represents the day when tumor volume reached $\sim 100 \text{ mm}^3$ after the inoculation of cells and the treatment started; $***P < 0.001$ represents control vs AA-NLC-TF, and $**P < 0.05$ represents NLC-TF vs AA-NLC-TF.)

10C,D the difference in the fluorescence intensity between groups treated with nontargeted and targeted nanoparticles was due to the differential distribution of nanoparticles. Bright red emission (Figure 10C) and higher fluorescence intensity (Figure 10F) of targeted nanoparticles (AA-NLC-TF) in the tumor than other organs were due to active tumor-targeting ability of the nanoparticles bearing AA ligand. However, relatively weak fluorescence of NLC-TF nanoparticles at the tumor site and high fluorescence in other major organs were attributed to their nontargetability and systemic distribution. This demonstrated the specific targeting ability of AA-NLC-TF to the tumor that contains sigma receptor-overexpressed cancer cells in a living body.

3.14. In Vivo Antitumor Efficacy. Benefiting from the cancer cell-specific internalization, 4T1 breast carcinoma-bearing mice were used to evaluate the antitumor efficacy of AA-NLC-TF NPs in vivo compared to NLC-TF, free FMN, and control. The 4T1 cells closely resemble human-derived metastatic breast cancer cell line MDA-M 231. Both the cell lines are estrogen-independent breast cancer cell lines and express sigma receptors and therefore 4T1 cells could be used as a suitable in vivo model for the evaluation of anticancer efficacy of NLC formulations.⁴⁶ Treatment was started when the tumor volume reached 100 mm^3 in all of the animals. Each group received iv dose of 10 mg/kg FMN equivalent every 2

days for seven times. As shown in the tumor volume curve in Figure 11A and tumor photographs in Figure 11B, the tumor volume of the control group treated with blank NLC NPs increased significantly, whereas that of the AA-NLC-TF-treated tumors showed almost no growth. The average tumor volume of the free FMN-treated groups was smaller than that of the control group, and the tumor volume of the AA-NLC-TF group was significantly smaller than that of both the NLC-TF-treated group ($P < 0.001$) and the control group ($P < 0.05$). At the end of the tumor regression study, tumors were excised and the average weight of the tumors was assessed (Figure 11C); the tumor inhibition rates of free FMN-, NLC-TF-, and AA-NLC-TF-treated groups were 29.50, 58.75, and 79.00% respectively. The tumor weight of the AA-NLC-TF-treated group at the end of the tumor regression study was 4.76-fold lower than the control group and 3.35-fold lower than the free FMN group. The results indicated that the active targeting of FMN in NLC NPs form improved its anticancer efficacy compared to the free form of FMN. For evaluating the safety of the formulation, body weight of all of the treated groups was determined. Compared to the control mice, weights of the NLC formulations and free FMN-treated mice remained almost unchanged, which indicate the in vivo biocompatibility of the NLC NPs and use of this nanoparticles as a safe bioagent.

3.15. Survival Analysis. The Kaplan–Meier survival plot in Figure 11D showed the median survival rate of all of the treated groups. Survival studies were performed for 30 days after the treatment of mice. The median survival of NLC-TF was 27 days significantly longer than the control group (median survival, 18 days) and free FMN-treated mice (median survival, 21 days). Treatment with FMN increased the survival time of the mice by 3 days compared to control. However, the median survival rate of targeted AA-NLC-TF NPs prolonged the survival of mice (median survival, >30 days), which indicated the improved efficacy of FMN by the targeted delivery system.

4. CONCLUSIONS

Sigma receptor-targeted AA-NLC-TF combines a unique AIE effect with the controlled release of the chemotherapeutic agent FMN. To the best of our knowledge, this is the first report of liquid crystalline phase particles loaded with FMN for the treatment of breast cancer. This theranostic approach not only reports the location of the tumor by AIE effects, but also facilitates intracellular drug release following receptor-mediated endocytosis for optimized therapeutic effect. Furthermore, strategic use of high lipid volume fractioned liquid crystalline particles circumvent the poor solubility issue of FMN, which results in high loading. Our results demonstrated the specific binding of AA-NLC-TF to sigma receptor positive MDA-MB 231 and 4T1 cells, and systemic delivery of AA-NLC-TF significantly inhibited tumor growth in a 4T1-induced breast cancer xenograft model. Moreover, we showed that targeted delivery of AA-NLC-TF and the presence of tumor could be detected noninvasively by the active AIE imaging in comparison to nontargeted NLC-TF nanoparticles. Conclusively, aggregation-induced emission fluorogen-based nanotheranostics developed in this study could be a promising platform for imaging and targeted noninvasive oncotherapy.

■ ASSOCIATED CONTENT

Supporting Information

The Supporting Information is available free of charge on the ACS Publications website at DOI: 10.1021/acsami.7b19109.

Synthesis of Pluronic F127–anisamide conjugate (PF127-AA), quantification of FMN and TPE by HPLC method, hemolysis assay, cytotoxicity of blank and AA-NLC-TF NPs particles on J774.2 cells, uptake of NLC NPs in 4T1 cells after treatment for 12 h, and ROS activity in MDA-MB 231 after treatment with free FMN, NLC-TF, and AA-NLC-TF for 12 and 24 h (PDF)

■ AUTHOR INFORMATION

Corresponding Author

*E-mail: prabhat_mishra@cdri.res.in, mishrapr@hotmail.com. Phone: +91-522-2612411(4537). Fax: +91-522-2623405.

ORCID

Sandeep Urandur: 0000-0001-5803-077X
Pratibha Ramarao: 0000-0001-6666-5417
Prabhat Ranjan Mishra: 0000-0002-7418-8283

Notes

The authors declare no competing financial interest.
CDRI communication number for this manuscript is 9667.

■ ACKNOWLEDGMENTS

The authors acknowledge CSIR, New Delhi, for providing research fellowship and required funds (ESC0103) and CSIR-CDRI for research facilities. They thank A.L. Vishwakarma and Madhu Chaturvedi for assisting with flow cytometer experiments and Dr. Kavita Singh for contribution in CLSM Facility at Electron Microscopy Division CDRI. The authors also thank V.A. Raghunathan for providing SAXS facility, Raman Research Institute, Bangalore, and K.M. Yatheendran for his technical help in CRYO-FESEM analysis, Raman Research Institute, Bangalore. They are grateful to Dr. Ramakrishna Rachumallu, Dr. Shweta Sharma, and Durga Prasad Yarra for useful discussion.

■ REFERENCES

- (1) Kerlikowske, K.; Zhu, W.; Tosteson, A. N. A.; et al. Identifying women with dense breasts at high risk for interval cancer: A cohort study. *Ann. Intern. Med.* **2015**, *162*, 673–681.
- (2) Oeffinger, K. C.; Fontham, E. T. H.; Etzioni, R.; et al. Breast cancer screening for women at average risk: 2015 guideline update from the American Cancer Society. *J. Am. Med. Assoc.* **2015**, *314*, 1599–1614.
- (3) Scheel, J. R.; Lee, J. M.; Sprague, B. L.; Lee, C. I.; Lehman, C. D. Screening Ultrasound as an Adjunct to Mammography in Women with Mammographically Dense Breasts. *Am. J. Obstet. Gynecol.* **2015**, *212*, 9–17.
- (4) Wu, T.-J.; Tzeng, Y.-K.; Chang, W.-W.; Cheng, C.-A.; Kuo, Y.; Chien, C.-H.; Chang, H.-C.; Yu, J. Tracking the engraftment and regenerative capabilities of transplanted lung stem cells using fluorescent nanodiamonds. *Nat. Nanotechnol.* **2013**, *8*, 682–689.
- (5) Gao, X.; Cui, Y.; Levenson, R. M.; Chung, L. W. K.; Nie, S. In vivo cancer targeting and imaging with semiconductor quantum dots. *Nat. Biotechnol.* **2004**, *22*, 969.
- (6) Oh, E.; Liu, R.; Nel, A.; Gemill, K. B.; Bilal, M.; Cohen, Y.; Medintz, I. L. Meta-analysis of cellular toxicity for cadmium-containing quantum dots. *Nat. Nanotechnol.* **2016**, *11*, 479–486.
- (7) Wang, D.; Qian, J.; He, S.; Park, J. S.; Lee, K.-S.; Han, S.; Mu, Y. Aggregation-enhanced fluorescence in PEGylated phospholipid nanomicelles for in vivo imaging. *Biomaterials* **2011**, *32*, 5880–5888.
- (8) Han, X.; Liu, D.-E.; Wang, T.; Lu, H.; Ma, J.; Chen, Q.; Gao, H. Aggregation-Induced-Emissive Molecule Incorporated into Polymeric Nanoparticulate as FRET Donor for Observing Doxorubicin Delivery. *ACS Appl. Mater. Interfaces* **2015**, *7*, 23760–23766.
- (9) Caltagirone, C.; Arca, M.; Falchi, A. M.; Lippolis, V.; Meli, V.; Monduzzi, M.; Nylander, T.; Rosa, A.; Schmidt, J.; Talmon, Y.; Murgia, S. Solvatochromic fluorescent BODIPY derivative as imaging agent in camptothecin loaded hexosomes for possible theranostic applications. *RSC Adv.* **2015**, *5*, 23443–23449.
- (10) Meli, V.; Caltagirone, C.; Sinico, C.; Lai, F.; Falchi, A. M.; Monduzzi, M.; Obiols-Rabasa, M.; Picci, G.; Rosa, A.; Schmidt, J.; et al. Theranostic hexosomes for cancer treatments: an in vitro study. *New J. Chem.* **2017**, *41*, 1558–1565.
- (11) Nilsson, C.; Barrios-Lopez, B.; Kallinen, A.; Laurinmäki, P.; Butcher, S. J.; Raki, M.; Weisell, J.; Bergström, K.; Larsen, S. W.; Østergaard, J.; et al. SPECT/CT imaging of radiolabeled cubosomes and hexosomes for potential theranostic applications. *Biomaterials* **2013**, *34*, 8491–8503.
- (12) Szlezak, M.; Nieciecka, D.; Joniec, A.; Pękala, M.; Gorecka, E.; Emo, M.; Stébé, M. J.; Krysiński, P.; Bilewicz, R. Monoolein Cubic Phase Gels and Cubosomes Doped with Magnetic Nanoparticles—Hybrid Materials for Controlled Drug Release. *ACS Appl. Mater. Interfaces* **2017**, *9*, 2796–2805.
- (13) Rodrigues, L.; Kyriakos, K.; Schneider, F.; Dietz, H.; Winter, G.; Papadakis, C. M.; Hubert, M. Characterization of lipid-based hexosomes as versatile vaccine carriers. *Mol. Pharmaceutics* **2016**, *13*, 3945–3954.

- (14) Suga, K.; Kondo, D.; Otsuka, Y.; Okamoto, Y.; Umakoshi, H. Characterization of aqueous oleic acid/oleate dispersions by fluorescent probes and Raman spectroscopy. *Langmuir* **2016**, *32*, 7606–7612.
- (15) Zhu, Z.; Qian, J.; Zhao, X.; Qin, W.; Hu, R.; Zhang, H.; Li, D.; Xu, Z.; Tang, B. Z.; He, S. Stable and Size-Tunable Aggregation-Induced Emission Nanoparticles Encapsulated with Nanographene Oxide and Applications in Three-Photon Fluorescence Bioimaging. *ACS Nano* **2016**, *10*, 588–597.
- (16) Han, K.; Wang, S.-B.; Lei, Q.; Zhu, J.-Y.; Zhang, X.-Z. Ratiometric Biosensor for Aggregation-Induced Emission-Guided Precise Photodynamic Therapy. *ACS Nano* **2015**, *9*, 10268–10277.
- (17) Mei, J.; Leung, N. L. C.; Kwok, R. T. K.; Lam, J. W. Y.; Tang, B. Z. Aggregation-Induced Emission: Together We Shine, United We Soar! *Chem. Rev.* **2015**, *115*, 11718–11940.
- (18) Liu, J.; Chen, C.; Ji, S.; Liu, Q.; Ding, D.; Zhao, D.; Liu, B. Long wavelength excitable near-infrared fluorescent nanoparticles with aggregation-induced emission characteristics for image-guided tumor resection. *Chem. Sci.* **2017**, *8*, 2782–2789.
- (19) RamaKrishna, N. V. S.; Devanesan, P. D.; Rogan, E. G.; Cavalieri, E. L.; Jeong, H.; Jankowiak, R.; Small, G. J. Mechanism of metabolic activation of the potent carcinogen 7,12-dimethylbenz[a]-anthracene. *Chem. Res. Toxicol.* **1992**, *5*, 220–226.
- (20) Xu, G.; Lin, G.; Lin, S.; Wu, N.; Deng, Y.; Feng, G.; Chen, Q.; Qu, J.; Chen, D.; Chen, S.; et al. The Reproductive Toxicity of CdSe/ZnS Quantum Dots on the in vivo Ovarian Function and in vitro Fertilization. *Sci. Rep.* **2016**, *6*, No. 37677.
- (21) Aldred, M. P.; Li, C.; Zhu, M.-Q. Optical Properties and Photo-Oxidation of Tetraphenylethene-Based Fluorophores. *Chem. – Eur. J.* **2012**, *18*, 16037–16045.
- (22) Zhu, Z.; Song, B.; Yuan, J.; Yang, C. Enabling the Triplet of Tetraphenylethene to Sensitize the Excited State of Europium(III) for Protein Detection and Time-Resolved Luminescence Imaging. *Adv. Sci.* **2016**, *3*, No. 1600146.
- (23) Yu, G.; Cook, T. R.; Li, Y.; Yan, X.; Wu, D.; Shao, L.; Shen, J.; Tang, G.; Huang, F.; Chen, X.; Stang, P. J. Tetraphenylethene-based highly emissive metallacage as a component of theranostic supramolecular nanoparticles. *Proc. Natl. Acad. Sci. U.S.A.* **2016**, *113*, 13720–13725.
- (24) Dasargyri, A.; Hervella, P.; Christiansen, A.; Proulx, S. T.; Detmar, M.; Leroux, J.-C. Findings questioning the involvement of Sigma-1 receptor in the uptake of anisamide-decorated particles. *J. Controlled Release* **2016**, *224*, 229–238.
- (25) Aydar, E.; Onganer, P.; Perrett, R.; Djamgoz, M. B.; Palmer, C. P. The expression and functional characterization of sigma (σ) 1 receptors in breast cancer cell lines. *Cancer Lett.* **2006**, *242*, 245–257.
- (26) Ramya, A. N.; Joseph, M. M.; Nair, J. B.; Karunakaran, V.; Narayanan, N.; Maiti, K. K. New insight of tetraphenylethylene-based Raman signatures for targeted SERS nanoprobe construction toward prostate cancer cell detection. *ACS Appl. Mater. Interfaces* **2016**, *8*, 10220–10225.
- (27) Zhang, S.; Tang, X.; Tian, J.; Li, C.; Zhang, G.; Jiang, W.; Zhang, Z. Cardioprotective effect of sulphonated formononetin on acute myocardial infarction in rats. *Basic Clin. Pharmacol. Toxicol.* **2011**, *108*, 390–395.
- (28) Gautam, J.; Khedgikar, V.; Kushwaha, P.; Choudhary, D.; Nagar, G. K.; Dev, K.; Dixit, P.; Singh, D.; Maurya, R.; Trivedi, R. Formononetin, an isoflavone, activates AMP-activated protein kinase/ β -catenin signalling to inhibit adipogenesis and rescues C57BL/6 mice from high-fat diet-induced obesity and bone loss. *Br. J. Nutr.* **2017**, *117*, 645–661.
- (29) Vitale, D. C.; Piazza, C.; Melilli, B.; Drago, F.; Salomone, S. Isoflavones: estrogenic activity, biological effect and bioavailability. *Eur. J. Drug Metab. Pharmacokinet.* **2013**, *38*, 15–25.
- (30) Singh, S. P.; Wahajuddin, M.; Tewari, D.; Pradhan, T.; Jain, G. K. PAMPA permeability, plasma protein binding, blood partition, pharmacokinetics and metabolism of formononetin, a methoxylated isoflavone. *Food Chem. Toxicol.* **2011**, *49*, 1056–1062.
- (31) Tolleson, W. H.; Doerge, D. R.; Churchwell, M. I.; Marques, M. M.; Roberts, D. W. Metabolism of biochanin A and formononetin by human liver microsomes in vitro. *J. Agric. Food Chem.* **2002**, *50*, 4783–4790.
- (32) Wang, X.; Yang, Y.; Zhuang, Y.; Gao, P.; Yang, F.; Shen, H.; Guo, H.; Wu, D. Fabrication of pH-responsive nanoparticles with an AIE feature for imaging intracellular drug delivery. *Biomacromolecules* **2016**, *17*, 2920–2929.
- (33) Garti, N. *Self-Assembled Supramolecular Architectures: Lyotropic Liquid Crystals*; John Wiley & Sons, 2012; Vol. 3.
- (34) Muller, F.; Salonen, A.; Glatter, O. Phase behavior of Phytantriol/water bicontinuous cubic Pn3m cubosomes stabilized by Laponite disc-like particles. *J. Colloid Interface Sci.* **2010**, *342*, 392–398.
- (35) Sharma, S.; Verma, A.; Singh, J.; Teja, B. V.; Mittapelly, N.; Pandey, G.; Urundur, S.; Shukla, R. P.; Konwar, R.; Mishra, P. R. Vitamin B6 Tethered Endosomal pH Responsive Lipid Nanoparticles for Triggered Intracellular Release of Doxorubicin. *ACS Appl. Mater. Interfaces* **2016**, *8*, 30407–30421.
- (36) Verma, A.; Sharma, S.; Gupta, P. K.; Singh, A.; Teja, B. V.; Dwivedi, P.; Gupta, G. K.; Trivedi, R.; Mishra, P. R. Vitamin B12 functionalized layer by layer calcium phosphate nanoparticles: A mucoadhesive and pH responsive carrier for improved oral delivery of insulin. *Acta Biomater.* **2016**, *31*, 288–300.
- (37) Dian, L.; Yang, Z.; Li, F.; Wang, Z.; Pan, X.; Peng, X.; Huang, X.; Guo, Z.; Quan, G.; Shi, X.; Chen, B.; Li, G.; Wu, C. Cubic phase nanoparticles for sustained release of ibuprofen: formulation, characterization, and enhanced bioavailability study. *Int. J. Nanomed.* **2013**, *8*, 845–854.
- (38) Nasr, M.; Dawoud, M. Sorbitol based powder precursor of cubosomes as an oral delivery system for improved bioavailability of poorly water soluble drugs. *J. Drug Delivery Sci. Technol.* **2016**, *35*, 106–113.
- (39) Thapa, R. K.; Choi, J. Y.; Poudel, B. K.; Hiep, T. T.; Pathak, S.; Gupta, B.; Choi, H.-G.; Yong, C. S.; Kim, J. O. Multilayer-coated liquid crystalline nanoparticles for effective sorafenib delivery to hepatocellular carcinoma. *ACS Appl. Mater. Interfaces* **2015**, *7*, 20360–20368.
- (40) Sharma, S.; Singh, J.; Verma, A.; Teja, B. V.; Shukla, R. P.; Singh, S. K.; Sharma, V.; Konwar, R.; Mishra, P. Hyaluronic acid anchored paclitaxel nanocrystals improves chemotherapeutic efficacy and inhibits lung metastasis in tumor-bearing rat model. *RSC Adv.* **2016**, *6*, 73083–73095.
- (41) Ma, X.; Tao, H.; Yang, K.; Feng, L.; Cheng, L.; Shi, X.; Li, Y.; Guo, L.; Liu, Z. A functionalized graphene oxide–iron oxide nanocomposite for magnetically targeted drug delivery, photothermal therapy, and magnetic resonance imaging. *Nano Res.* **2012**, *5*, 199–212.
- (42) Driever, C. D.; Mulet, X.; Waddington, L. J.; Postma, A.; Thissen, H.; Caruso, F.; Drummond, C. J. Layer-by-layer polymer coating on discrete particles of cubic lyotropic liquid crystalline dispersions (cubosomes). *Langmuir* **2013**, *29*, 12891–12900.
- (43) Boyd, B. J.; Rizwan, S. B.; Dong, Y.-D.; Hook, S.; Rades, T. Self-Assembled Geometric Liquid-Crystalline Nanoparticles Imaged in Three Dimensions: Hexosomes Are Not Necessarily Flat Hexagonal Prisms. *Langmuir* **2007**, *23*, 12461–12464.
- (44) Rizwan, S. B.; Dong, Y. D.; Boyd, B. J.; Rades, T.; Hook, S. Characterisation of bicontinuous cubic liquid crystalline systems of phytantriol and water using cryo field emission scanning electron microscopy (cryo FESEM). *Micron* **2007**, *38*, 478–485.
- (45) Wu, X. Y.; Xu, H.; Wu, Z. F.; Chen, C.; Liu, J. Y.; Wu, G. N.; Yao, X. Q.; Liu, F. K.; Li, G.; Shen, L. Formononetin, a novel FGFR2 inhibitor, potentially inhibits angiogenesis and tumor growth in preclinical models. *Oncotarget* **2015**, *6*, 44563.
- (46) Ma, G.; He, J.; Yu, Y.; Xu, Y.; Yu, X.; Martinez, J.; Lonard, D. M.; Xu, J. Tamoxifen Inhibits ER-negative Breast Cancer Cell Invasion and Metastasis by Accelerating Twist1 Degradation. *Int. J. Biol. Sci.* **2015**, *11*, 618–628.